

University of Exeter May 2013
ECMM102 Group Project

Modelling the response of the Built Environment to climate change:

CFD modelling of buoyancy-driven flow around a simplified human form in a naturally ventilated room

580009756 Individual Report 2

Acknowledgements:

I would like to thank Dr Gavin Tabor for his continued guidance throughout the project, and also to Dr Matthew Eames and Edward Shorthouse for attending and advising at the weekly group meetings.

Abstract

In view of the significant effect of climate change on human society with increasing urbanisation, there is considerable scope for building design to reduce the effects of temperature extremes. In recent decades, heating, ventilating and air conditioning systems which consume large amounts of energy have become a necessity. Consequently, natural ventilation systems are increasingly being incorporated into modern buildings and this study is concerned with the computational fluid dynamics modelling of a human situated in a room. This project is part of a group project and is primarily concerned with providing accurate simulations of the flow near the surface of the human which is affected by turbulence in the boundary layer. Of particular importance is the choice of turbulence model because of the low flow rates in the boundary layer and in this study the standard $k-\epsilon$ with enhanced wall treatment was compared with the SST $k-\omega$ model. There are two main aspects of natural ventilation systems: the first concerns the comfort of an individual human being, and the second is the harnessing of the buoyancy force which drives the flow. A continuous surface model design of the human was developed in order to ensure the mesh was capable of solution in a reasonable time. In future studies, the results of simulations from a segmented design with different temperatures at specific parts of the human body can be compared with the flow predicted using an average temperature for the whole human surface.

Table of Contents

1	Introduction	1
2	Review of previous work	1
2.1	Climate change	1
2.2	Natural ventilation	2
2.3	Design and CFD of the human form	3
2.4	Turbulence models.....	5
2.5	Cylinder in cross flow.....	6
2.6	IESD-Fiala model	7
3	Theory	7
3.1	Dimensionless number groups.....	7
3.2	The Boussinesq approximation for buoyancy-driven flow	9
3.3	Boundary layer growth and separation	10
3.4	Turbulence models.....	11
3.4.1	Standard k- ϵ model.....	12
3.4.2	k- ω model and the SST modification	12
3.5	Wall Treatment	12
4	Methodologies.....	15
4.1	Project management.....	15
4.2	Literature research	17
4.3	Theory concepts.....	17
4.4	Different geometry designs.....	17
4.5	CFD in ANSYS	17
4.6	David Laserscanner	17
4.7	Thermal imaging camera	17
4.8	Interlinking with the other sub-groups	18
5	Design	18
5.1	Human forms	18
5.1.1	Cylinder.....	18
5.1.2	Initial design	19
5.1.3	Human form	19
5.1.4	Basic Manikin.....	19
5.1.5	Detailed Manikin.....	19
5.1.6	Human scan	19
5.2	Integration with room 170 model	20

6	CFD	21
6.1	Initial CFD	21
6.2	Human form	23
6.2.1	Mesh generation	24
6.2.2	Fluent set-up	25
6.2.3	Results	26
6.3	Harrison room 170	30
6.3.1	Mesh creation	31
6.3.2	Fluent set-up	31
6.3.3	Results	32
6.4	Sources of error	33
7	Analysis and discussion	34
8	Conclusions	35
9	References	I
10	Appendices	IV
10.1	Appendix A: set-up of Linux-based computers	IV
10.2	Appendix B: risk assessment for use of line-laser	V
10.3	Appendix C: using the David Laserscanner software	VI
10.4	Appendix D: sustainability and economic benefit	VI

Table of Figures

Figure 2.1: showing velocity vectors and surface temperatures for a human [8]	3
Figure 2.2: showing the Loughborough paper figure 7 [8]	3
Figure 2.3: thermal plume from a vase-like geometry [13]	5
Figure 2.4: wake profiles for low Reynolds numbers [16]	6
Figure 3.1: boundary layer transition from laminar to turbulent [31] [32]	11
Figure 3.2: graph of u^+ against y^+ for a boundary layer [35]	13
Figure 4.1: project Gantt chart	16
Figure 5.1: initial design	18
Figure 5.2: human form	18
Figure 5.3: basic Manikin	18
Figure 5.4: detailed Manikin	18
Figure 5.5: human scan	18
Figure 5.6: Harrison room 170 inverted model with human form	20
Figure 6.1: initial design meshed using the settings in Table 6.1 (left), close-up view of the boundary layer mesh (right)	22
Figure 6.2: contours of velocity mag. [ms^{-1}] for the initial CFD (left), pathlines coloured by velocity mag. [ms^{-1}] (right)	23
Figure 6.3: mesh for the head of the human form	24
Figure 6.4: contours of velocity mag. [ms^{-1}] for Run 2 at the symmetry plane (left), close-up view of head (right)	27
Figure 6.5: contours of velocity mag. [ms^{-1}] for Run 5 at the symmetry plane	27
Figure 6.6: contours of velocity mag. [ms^{-1}] for Run 2 at inlet/outlet plane	28
Figure 6.7: contours of total temperature [K] for Run 2	28
Figure 6.8: contours of total temperature [K] for Run 5	29
Figure 6.9: histogram of wall y^+ values for Run 2	29
Figure 6.10: histogram of wall y^+ values for Run 5	30
Figure 6.11: cross-section view of the mesh at the inlet vents	31
Figure 6.12: contours of velocity mag. [ms^{-1}] for standard k- ϵ model at inlet plane	32
Figure 6.13: contours of velocity mag. [ms^{-1}] for standard k- ϵ model at human plane	33
Figure 6.14: contours of total temperature [K] for standard k- ϵ model at inlet plane	33
Figure 10.1: David Laserscanner calibration	VI
Figure 10.2: lines indicating detected surfaces coloured by distance from the camera (left); final aligned scan using several angles of the miniature Manikin (right)	VI

List of Tables

Table 6.1: optimum mesh settings	21
Table 6.2: optimum mesh statistics.....	22
Table 6.3: mesh settings for human form	24
Table 6.4: mesh statistics for human form.....	24
Table 6.5: properties of air [38]	25
Table 6.6: calculated values of the dimensionless groups	25
Table 6.7: boundary conditions used in simulations.....	25
Table 6.8: results for human form simulations	26
Table 6.9: room 170 inlet velocity calculation	30
Table 6.10: mesh settings for room 170.....	31
Table 6.11: mesh statistics for room 170	31
Table 6.12: room 170 temperatures recorded by the sensor sub-group	32

1 Introduction

The objective of the whole project was to explore computational fluid dynamics (CFD) modelling of buildings and humans to identify how this modelling could be used to predict the responses to future weather conditions.

The project was divided into three sub-groups: the first to analyse the room as a whole, the second to concentrate on the human and surrounding volume, and the third to investigate the sensor devices and electronics necessary to record data for the environmental conditions in the room. This section of the project is concerned with design of the human form, in order to model the temperature and airflow in the volume surrounding the human.

The objectives of this section of the group project were as follows:

- Produce a range of basic to complex human CAD geometries
- Create a high accuracy mesh around a human form in a control volume
- Run buoyancy-driven simulations using ANSYS Fluent
- Integration of the high accuracy mesh produced for the human form into a room

2 Review of previous work

2.1 Climate change

Changes in the outdoor environment are largely influenced by the position of the sun relative to the Earth and the human position on the Earth. In addition to the shorter term daily and seasonal variations there are much longer cycles of change which are related to variations in the tilt of the Earth's axis relative to the plane of its orbit round the sun and the fact that this orbit is elliptical with the sun at one focus. It is these factors which are understood to have created the series of ice ages which have been determined from geological studies [1]. As recently as the mid-fifteenth to mid-nineteenth centuries, there was significant global cooling creating the "little ice age". Paintings of people playing on the frozen Thames are perhaps the best illustration of this.

However, in recent decades another significant trend of increase in global temperatures has been detected and which is generally believed to be a consequence of the increasing levels of carbon dioxide and other greenhouse gases emitted by power stations, factories, motor transport and the heating and cooling of buildings since industrialisation began. This global warming is what has come to be known as climate change.

Recent predictions, based on the assumptions in a medium emission scenario, are that there is a 50% probability that by 2100 there will be an increase of 2.4 – 4.8°C on the hottest summer day in Britain, depending on location and relative to a 1961 – 1990 baseline [2].

In view of the significant effect of climate change on human society, and now that over half the world's population lives in cities, there is considerable scope for building design to either ameliorate or exacerbate the effects of temperature extremes.

The increase of the thermal load in buildings due to the arrival of office computers and lighting requirements, led to the installation of air conditioning systems necessary to neutralise these loads and to create a good indoor thermal comfort. Heating, ventilating, air-conditioning (HVAC) systems, which consume large quantities of energy, therefore became a necessity for almost all buildings [3].

According to the Fourth Assessment Report of the Intergovernmental Panel on Climate Change (IPCC), the buildings sector has the greatest potential for climate change mitigation. In order to investigate the performance of buildings in a future warmer climate, the IPCC published a set of emission scenarios for use in climate change codes with a focus on the reduction of greenhouse gas emissions. Studies lead to two main conclusions: cooling loads are likely to increase from 50 to over 90% until the end of the century and optimisation potential is strongly related to building properties [4].

2.2 Natural ventilation

Natural ventilation systems, as opposed to mechanical HVAC systems, are increasingly being used by designers of modern buildings. This is in response to environmental concerns together with the demands for energy efficiency, along with the increasing cost of fuel for heating and air conditioning [5]. Highly insulated offices require minimal heating in the winter, but the resultant fuel savings are offset by the cost of air conditioning in the summer [3].

The theory for buoyancy-driven ventilation was explained by Linden et al. [6] when considering displacement ventilation of a simple rectangular box. The heat source produces a rising plume of air which introduces fresh ambient air, taking it upwards into the upper region of space, where it is recirculated. As more and more light air accumulates in the upper region, the rising plume begins to displace this lighter air until a steady state is achieved. In the steady state space, the layer of buoyant air drives a flow through the upper openings since the hydrostatic pressure difference between the top and bottom of the layer is smaller inside the space than between the same heights outside the space. This causes fresh air to be drawn in through the lower openings [5].

The amount of outdoor air introduced into naturally ventilated offices will depend on various factors, including wind speed and direction, the air filters used and the cross section of inlets and outlets. Rooms with a natural and hybrid air conditioning system can expect to have large increases in the amount of outdoor air introduced which will significantly improve the air quality. Models for creating driven flow would also need to be considered in a comprehensive study.

The theory of buoyancy-driven flow is an important aspect of modelling natural convection, in particular the Boussinesq approximation which is the subject of section 3.2. The airflow velocities in this project are by their nature very small. Natural convection around a human body occurs by virtue of the different densities of the surrounding air which are influenced by relative temperatures of the different parts of the human body, for instance, the feet are generally colder than the chest [7].

Cropper et al. [8] carried out a study which included CFD simulations of a human body in a control volume with natural ventilation modelling the transfer of heat and the thermal plume. Figure 2.1 and Figure 2.2 show results from this study. The profile of the thermal plume is of particular relevance to this study.

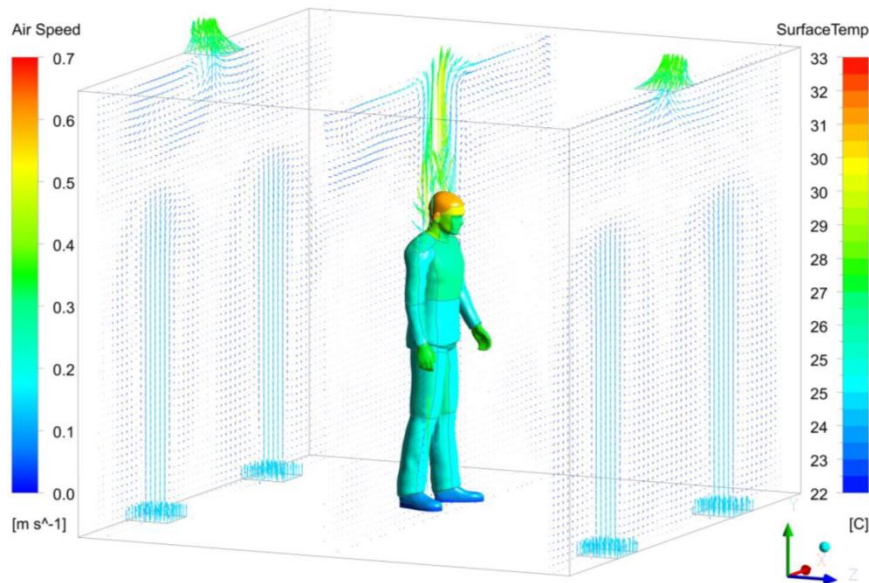


Figure 2.1: showing velocity vectors and surface temperatures for a human [8]

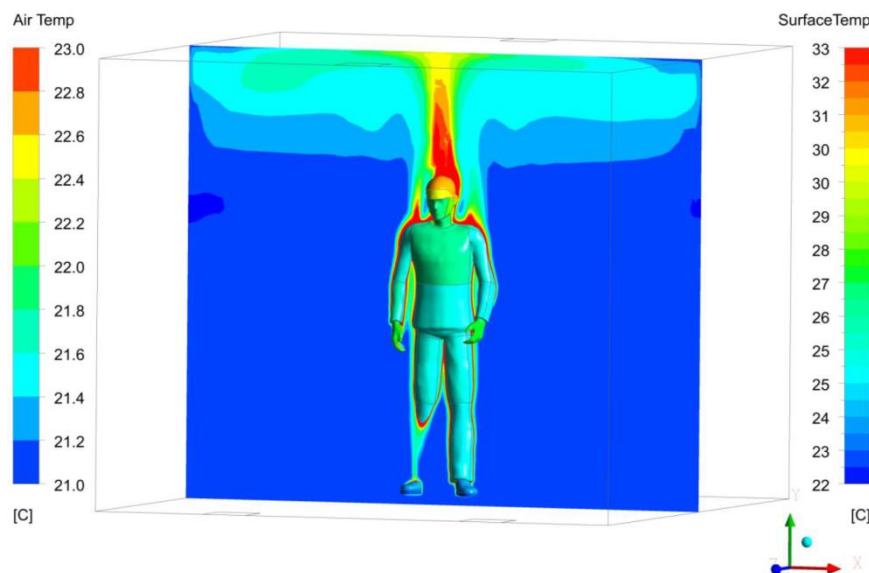


Figure 2.2: showing the Loughborough paper figure 7 [8]

2.3 Design and CFD of the human form

This section of the report discusses the initial research and investigation carried out in the areas of the human CAD geometry, the CFD analysis and the thermal comfort modelling.

During the last decade, CFD technology and the computing power available has progressed and made it possible to analyse the micro-climate around the human body [9]. By its nature, natural convection is less tightly controlled than air conditioning and so modelling the air flow requires the power of modern-day computers to produce the complex predictions needed.

The combination of CFD modelling and human response modelling enables the simulation of complex indoor environmental conditions on human comfort. CFD predicts detailed data for temperature and velocities of air flow around a human body, whilst a thermal comfort model is able to predict the response by a human body to the environment surrounding it. Coupling of the two models uses the output of one as the input of the other. The two-way data transfer is thought to be particularly important because of the effect that a human body has on the local environment.

The computational modelling required in this project has two distinct aspects: the environment and the human body. Comfort and heat stress research requires a comprehensive model of human thermoregulation. Various studies of heat regulation in the human body have been conducted and probably the best known of these was by Stolwijk [10] including one for NASA in conjunction with the manned space programme. This was followed by the Gagge two-node model but the IESD-Fiala model, as discussed in section 2.6, has been used in more recent research [8] and this has been extensively validated and was used in this group project.

First attempts at multi-mode human thermal simulations used segmentation of a body into geometric shapes whereas later studies used articulated thermal manikins to improve the resolution of the human form. To enable studies, thermal manikins were introduced over 50 years ago. Thermal manikins are heated dummies which were originally developed to measure the thermal insulation of clothing [7]. These were later developed as computational thermal manikins (CTMs).

Meshing a CAD model is by far the most time-consuming part of CFD analysis. Therefore from the point of view of computational expense, the geometry of the CTM should be as simple as possible, whereas from the point of view of simulation accuracy it should be as real as possible. For example, the hair and clothes are not included in most analysis since it would hugely increase the level of complexity [9].

Finding the critical point to achieve highest accuracy and minimise computational expense is normally done by way of a convergence study. This is where simulations using meshes of a range of numbers of cells, for example from 50,000 to 5,000,000, are run and certain properties of the fluid flow, for example mass flow rate, are plotted against number of cells.

The use of different levels of model complexity is justified by the approach of Nilsson [11], where three complexities are used: computer models, manikins and persons.

The level of geometric complexity of CTMs depends on the purpose of the simulations using them. Dunnett [12] proposed an elliptical cylinder to simulate a human in a standing person [7], therefore an appropriate start point for the geometry appeared to be the very basic model of a cylinder, representing the approximate human form. The height of most CTMs is about 1.65m with a maximum diameter of 0.3m [7].

Research produced the next level of model complexity; a vase-like shape whose essential feature is a smooth and slowly changing outline, without limbs, as in the study by Murakami et al. [13], shown in Figure 2.3.

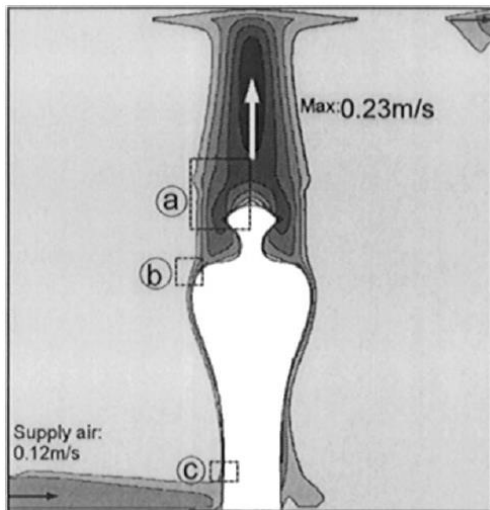


Figure 2.3: thermal plume from a vase-like geometry [13]

The research suggested that as regards the CFD, a ventilated room is usually divided into two parts: a cuboid enclosing the human body and the remaining room space. In order to accurately model the boundary layer around the CTM, an inflation mesh consisting of up to 20 layers emanating from the surface of the geometry should be created [7].

2.4 Turbulence models

Turbulence modelling is a crucial aspect of all CFD modelling, but is particularly important in buoyancy driven flows in which the buoyancy forces increase turbulent activity [5].

Although there are many turbulence models, it is an unfortunate fact that no single model is universally accepted as being superior to the others for all classes of problems. The choice of a turbulence model is a compromise which depends on considerations such as; the physics encompassed in the flow, the established practice for a specific class of problems, the level of accuracy required, the available computational resources, and the amount of time available for the simulation.

Buoyancy driven flows are notoriously difficult to model using CFD techniques for the following reasons: small driving forces lead to numerical instabilities and there is uncertainty regarding how to accurately model turbulence. A good example of buoyancy driven flow is displacement ventilation in which use is made of the buoyancy forces produced by naturally occurring heat sources such as occupants and equipment [5].

Research showed that the standard $k-\epsilon$ model was used in early studies, but as it was derived for fully turbulent flow, it is inappropriate for a buoyant flow [3]. However, the use of a wall treatment overcomes this difficulty and it is proposed to use the standard $k-\epsilon$ model with enhanced treatment in this section of the project. Some studies compared the standard $k-\epsilon$ model with the RNG $k-\epsilon$ model or the low Reynolds $k-\epsilon$ model to investigate their influence on computational accuracy. The latter is very useful for accurately predicting the pressure and convective heat transfer over the body surface which has a complicated shape [13]. The disadvantage of the low Reynolds $k-\epsilon$ model is that it may require large amounts of processing power and so take a long time to solve, because of the need for extremely fine mesh grids near the human body [7].

The k - ω model is one of the most commonly used turbulence models and this uses two extra transport equations to represent the turbulent properties of the flow [14].

The shear stress transport (SST) k - ω model uses the k - ω formulation throughout the boundary layer so that it can be used as a low Reynolds turbulence model [15]. It is accurate and robust but the non-dimensional distance y^+ must be less than 2 to resolve the boundary layer [8].

2.5 Cylinder in cross flow

The classical case of a cylinder in cross flow was originally researched in connection with the design of one of the early models, but other design research superseded this. However, the results of the research are included in this section because the close-up of the head in Figure 6.4 would appear to show a pair of vortices in the wake, above the head. At the lowest Reynolds numbers the flow is steady and symmetric and the wake is laminar. At slightly higher, but still low Reynolds numbers, a pair of vortices become fixed in the wake, Figure 2.4. The work by Chatterjee [16] is not wholly relevant in that it concerns wall bounded flow, but it has interesting information concerning heat transfer.

In addition to the symmetrical flow vortices were observed, the isotherms also appear symmetrical about the line of symmetry in the wake region. The plots revealed that the temperature contours became steeper in the near-wake region with increasing Reynolds number. The higher Reynolds number sets a higher temperature gradient, leading to enhanced heat transfer. At low Reynolds numbers, heat is transported predominantly through diffusion, whereas at higher Reynolds convective transport becomes dominant.

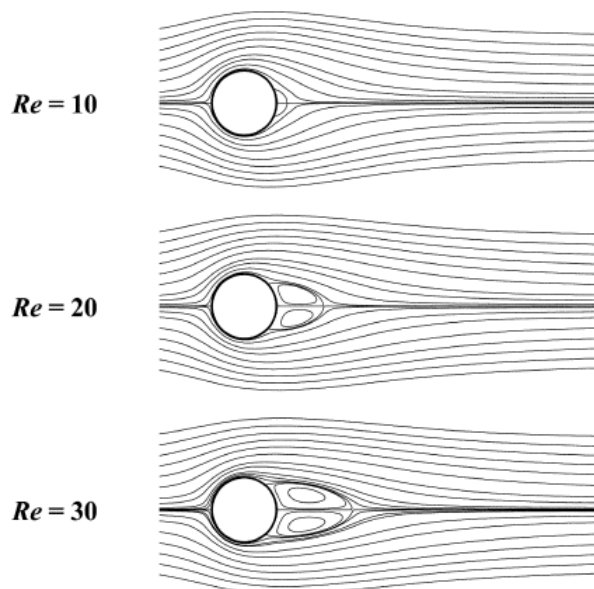


Figure 2.4: wake profiles for low Reynolds numbers [16]

2.6 IESD-Fiala model

The IESD-Fiala model is a human thermoregulation and thermal comfort model that incorporates both the controlling, active system and the controlled, passive one [17]. There are two aspects of modelling the human body: the four active responses to temperature; vasoconstriction, vasodilatation, sweating and shivering, and the passive system of heat passing through the body by conduction with heat balances as boundary conditions.

In previous work, the Fiala model has been coupled to a Fluent analysis [8]. There are two ways in which this type of coupling can be accomplished; by running models to completion each time before exchanging data or by exchanging data while one or both of the models are running. Both of the computer models calculate a result internally through an iterative process [18] [8].

In some cases of numerical prediction of thermal comfort, the body should be divided into many segments with each segment having its own boundary condition. For example, we may expect that the skin temperature of the feet and the chest are not the same and therefore should have different initial boundary conditions [7]. A goal for thermal comfort and heat stress researchers is to construct a comprehensive model of human thermoregulation. The completion of such a model requires radiative and convective heat transfer coefficients of individual body segments to be known [19].

In still air the human body is enclosed by a rising thermal plume due to the temperature difference between the body surface and ambient air. The thickness of this boundary layer around the human body increases with height and is similar to the flow around a vertical heated flat plate. Its thickness is about 8 cm at foot level and 15 cm at head height [20]. If the thermal plume is broken due to a high velocity of airflow impinging the human body the heat transfer coefficient increases greatly [7].

3 Theory

The topics covered in this section include those that were found to be necessary for an understanding of this project. They include the dimensionless numbers that were calculated to determine the characteristics of the flow around a human form, the Boussinesq approximation for buoyancy-driven flow, boundary layer growth and separation, together with several that are relevant to background knowledge and further development of the project. Turbulence models are also discussed but the choice of suitable models for comparison was determined by the literature review in chapter 2. The research of turbulence models also led to an understanding of how the models simulate the behaviour of boundary layers near walls, known as wall treatment or wall values.

3.1 Dimensionless number groups

There are various dimensionless numbers which are used in fluid and thermo dynamics and are relevant to this project. In addition to the Reynolds number, Re_L , the following will be used in one or more aspects of this project.

The Péclet number, Pe_L , is relevant to the study of transport phenomena in fluid flows and is defined as the ratio of the rate of advection to the rate of diffusion [21]. For diffusion of heat, i.e. thermal diffusion, the Péclet number is given by equation 3.1.

$$Pe_L = \frac{LU}{\alpha} = Re_L \cdot Pr \quad 3.1$$

where L is the characteristic length, U the velocity, α the thermal diffusivity given by equation 3.2, and Pr the Prandtl number, defined by equation below.

$$\alpha = \frac{k}{\rho c_p} \quad 3.2$$

where k is the thermal conductivity, ρ the density and c_p the specific heat capacity.

The Nusselt number, Nu_L , is defined as the ratio of convective to conductive heat transfer across a boundary [22], and is given by equation 3.3.

$$Nu_L = \frac{\text{convective heat transfer coefficient}}{\text{conductive heat transfer coefficient}} = \frac{hL}{k} \quad 3.3$$

where h is the convective heat transfer coefficient.

The Prandtl number, Pr , is defined as the ratio of momentum diffusivity to thermal diffusivity, as is given by equation 3.4 [23].

$$Pr = \frac{\nu}{\alpha} = \frac{\text{viscous diffusion rate}}{\text{thermal diffusion rate}} = \frac{c_p \mu}{k} \quad 3.4$$

where ν is the kinematic viscosity and μ is the dynamic viscosity.

The Rayleigh number, Ra_L , which is associated with buoyancy driven flow, indicates whether the heat transfer of a fluid is in the form of conduction when $Ra < 10^8$, or convection when $Ra_L > 10^8$ [9] [24], and is defined by equation 3.5. When a human body is in stagnant air, the Rayleigh number will reach approximately 4×10^9 at head level, assuming a difference between a typical average body surface temperature of 29°C and an ambient temperature of 20°C.

Therefore, in most cases, the airflow around the human body is turbulent or is in the transition zone and can be considered turbulent [7].

$$Ra_L = \frac{g\beta\Delta TL^3}{\nu\alpha} = Gr \cdot Pr \quad 3.5$$

where g is the acceleration due to gravity, β is the thermal expansion coefficient given by equation 3.6 [25] and ΔT is the difference in temperature between the surface of the object and the ambient temperature.

$$\beta = -\frac{1}{\rho} \frac{\partial \rho}{\partial T} \quad 3.6$$

The Grashof number, Gr_L , describes the transition from laminar to turbulent flow in terms of the ratio of the buoyancy to viscous forces acting on a fluid [26] [27], and is given by equation 3.7. Generally, when $Gr_L < 10^8$ the flow is laminar, and when $Gr_L > 10^{10}$ the flow is turbulent [19].

$$Gr_L = \frac{g\beta\Delta TL^3}{\nu^2} \quad 3.7$$

The importance of buoyancy forces in a mixed-convection flow can be measured by the ratio of the Grashof to Reynolds numbers [9], given by equation 3.8 below.

$$\frac{Gr_L}{Re_L^2} = \frac{g\beta\Delta TL}{U^2} \quad 3.8$$

where U is the flow velocity.

When this ratio approaches or exceeds unity, there are strong buoyancy contributions to the flow. Conversely, if the value is very small, buoyancy forces may be ignored in simulations. In pure natural convection, the strength of the buoyancy-induced flow is measured by the Rayleigh number [9].

Generally, the convective heat transfer from the human body to the surrounding environment is affected by several factors including clothes, body posture, temperature difference, air velocity, turbulence intensity and airflow direction [9].

3.2 The Boussinesq approximation for buoyancy-driven flow

It is common practice in the studies of thermal convection to simplify the compressible Navier-Stokes equations by using an approximation proposed by Boussinesq in 1903. The basis of the approximation is that in flows with little variation in temperature, but in which that temperature difference drives the motion through the buoyancy effect, the density also consequently varies little and so can be ignored except in the buoyancy term in the vertical equation of motion [28] [29]. Equations 3.9 and 3.10 give the vertical terms of the compressible Navier-Stokes equations.

$$\frac{\partial \rho}{\partial t} + \nabla \cdot \rho u = 0 \quad 3.9$$

$$\frac{\partial}{\partial t} \rho u + \nabla \cdot \rho u u = -\nabla p + \mu \nabla^2 u + f_y \quad 3.10$$

where $f_y = (\rho - \rho_0)g$ is the body force term, ρ_0 is the constant density of the flow and μ is the dynamic viscosity.

Since buoyancy forces depend on the density difference which itself depends on the temperature difference, then we can deal with buoyant flow by using equation 3.11, which is obtained by using the Boussinesq approximation in equation 3.12 [30].

$$(\rho - \rho_0)g \approx -\rho_0\beta(T - T_0)g \quad 3.11$$

$$\rho = \rho_0[1 - \beta(T - T_0)] \quad 3.12$$

where T_0 is the operating temperature.

Including this body force, we can solve the incompressible Navier-Stokes equations 3.13 and 3.14 instead, along with the temperature transport energy equation 3.15.

$$\nabla \cdot u = 0 \quad 3.13$$

$$\frac{\partial}{\partial t}u + \nabla \cdot uu = -\frac{1}{\rho}\nabla p + \nu \nabla^2 u + \beta(T - T_0)g \quad 3.14$$

$$\frac{\partial}{\partial t}T + \nabla \cdot uT = \alpha(T - T_0) \quad 3.15$$

The approximation is accurate as long as changes in actual density are small; specifically, the Boussinesq approximation is valid when $\beta(T - T_0) \ll 1$, which is equivalent to $(T - T_0) \ll 292$ K using $\beta = 0.00343$ for air. Consequently, this constraint will also apply to the Rayleigh and Grashof numbers.

3.3 Boundary layer growth and separation

The understanding of the boundary layer behaviour was important to this study because the change in air temperature, by conduction, occurs close to the surface of the human. Therefore understanding how the heat energy is transferred, producing the buoyancy effect discussed in section 2.2, is fundamental in producing an accurate model.

The theoretical thickness of the boundary layer was an important value to calculate because the inflation mesh around the surface of the human needed to be of an adequate resolution in order to define the flow in the boundary layer. An equation for the calculation of the turbulent boundary layer thickness, δ , is given equation 3.16 [31], though this is intended for use with a flat plate, as opposed with the curved surface of a human.

$$\delta = \frac{0.376x}{Re_x^{1/5}} \quad 3.16$$

The no-slip boundary condition at a wall results in the boundary layer forming between the wall and the free-stream which grows in thickness with increase length of the wall, in the direction of the flow. When the Reynolds number of the flow reaches 10^5 , using the distance from the beginning of the wall as the length scale x , the boundary layer will begin transition from laminar to turbulent.

Figure 3.1 (left) shows the transition of an initially laminar boundary layer and its subsequent growth and development to turbulent. There are three distinct regions of the boundary layer when it has become turbulent: an inner laminar sub-layer in contact with the surface, an outer layer where the flow obeys the log law, and in between a transition region. Methods of accurately modelling the boundary layer are discussed in section 3.5. Figure 3.1 (right) gives a representation of a uniform boundary layer thickness in the direction of the flow, with dashed lines representing the borders between ideal mesh cells.

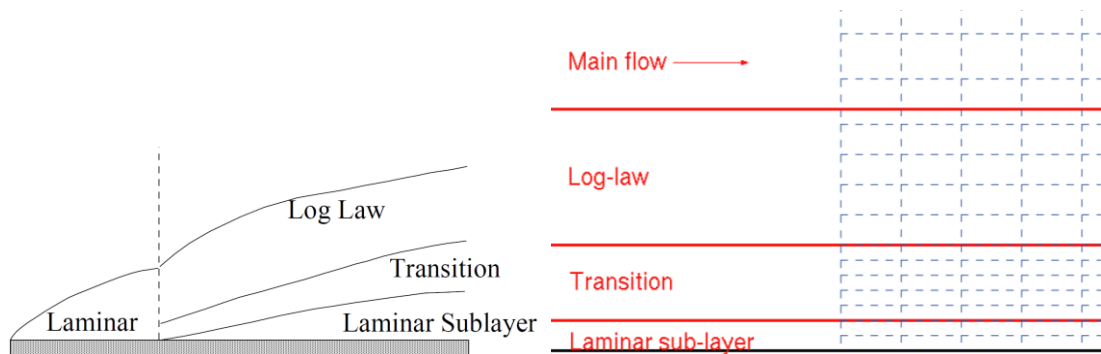


Figure 3.1: boundary layer transition from laminar to turbulent [31] [32]

The edge of the boundary layer with the free-stream is defined as the distance away from the wall at which point the velocity travelling parallel to the wall has reached 99% of the free-stream velocity.

3.4 Turbulence models

Turbulence models can be classified as follows [33]:

- Reynolds-Averaged Navier-Stokes (RANS) based models
 - Linear eddy-viscosity models
 - Algebraic models
 - One and two equation models
 - Non-linear eddy-viscosity models and algebraic stress models
 - Reynolds stress transport (RSM) models
- Large eddy simulation (LES)
- Detached eddy simulation (DES) and other hybrid models
- Direct numerical simulation (DNS)

The literature review concerning turbulence models, section 2.4, discussed a number of commonly used models. The following sub-sections give descriptions of the specific models used in this study, being only the two-equation RANS turbulence models. Low Reynolds models and the RNG k- ϵ model were not used. It is important to note that the Low Reynolds models are accessible through the command line function of Fluent, and not through the GUI as with the other turbulence models.

3.4.1 Standard k- ϵ model

The standard k- ϵ model is a two-equation model by which it is meant that it includes two extra transport equations to represent the turbulence of the flow. This enables the model to account for effects such as convection and diffusion of turbulent energy. The first variable is the turbulent kinetic energy, k , which determines the energy in the turbulence, and the second variable is the turbulent dissipation rate, ϵ . The second variable determines the scale of the turbulence [34].

3.4.2 k- ω model and the SST modification

In the k- ω model, the second transport variable is the specific dissipation rate, ω , which is defined by equation 3.17 [14]. Because this model uses the k- ω formulation in the inner parts of the boundary layer, it is directly usable all the way down to the wall surface, through the viscous sub-layer.

$$\omega = \frac{\epsilon}{k} \quad 3.17$$

A modification of the k- ω model is the shear-stress transport (SST) k- ω model. This combines the accurate boundary layer flow prediction of the k- ω model and then switches to k- ϵ behaviour in the free-stream and so avoids the problem that it is too sensitive to inlet free-stream turbulence properties [15].

An important consideration in the choice of turbulence model concerns the behaviour of the flow near a surface. This is discussed in detail in 3.5.

3.5 Wall Treatment

As stated in section 3.3, modelling the behaviour in the boundary layer is crucial to an accurate representation of buoyancy induced flow. This is because that is region where the heat transfer by conduction occurs.

The law of the wall is that the average velocity of a turbulent flow at any given point is proportional to the natural logarithm of the distance of that point from wall [35]. This law is applicable in the region of the turbulent boundary layer for values of $y^+ > 11.6$, where y^+ is the dimensionless wall distance defined by equation 3.19. This region is known as the log law region.

Below the log law region, nearest to the wall, is the viscous sub-layer and in that region the flow in the boundary layer follows the equation $u^+ = y^+$. This is accurate for regions in which $y^+ < 5$.

Between the two layers is the buffer layer $5 < y^+ < 11.6$ and in simulations of flow, a method has to be found for bridging this region. In CFD studies, this is achieved by adopting an appropriate turbulence model.

The red line of Figure 3.2 is a plot of values obtained experimentally for the behaviour in the boundary layer. It closely follows the line $u^+ = y^+$ for regions in the viscous sub-layer and the log law, equation 3.18, in the region known as the log law region.

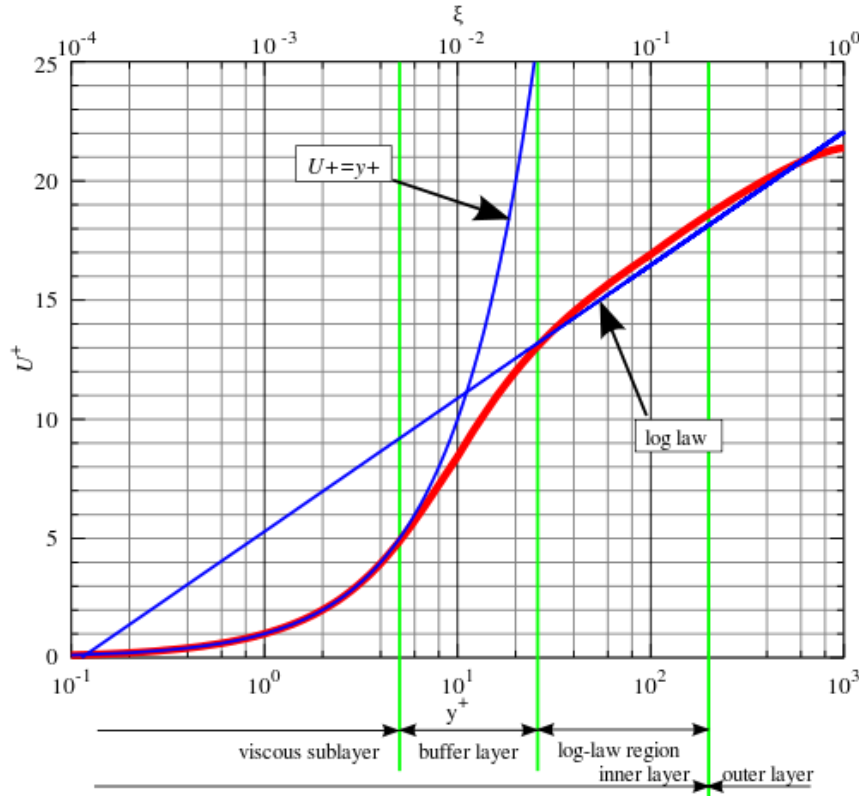


Figure 3.2: graph of u^+ against y^+ for a boundary layer [35]

$$u^+ = \frac{1}{\kappa} \ln(y^+) + C^+ \quad 3.18$$

where y^+ is the dimensionless wall distance, defined by equation 3.19, u^+ is the dimensionless velocity, defined by equation 3.20, $\kappa \approx 0.41$ is von Karman's constant and $C^+ \approx 5.1$, both of which are found experimentally.

$$y^+ = \frac{yu_\tau}{\nu} \quad 3.19$$

$$u^+ = \frac{u}{u_\tau} \quad 3.20$$

where u_τ is the friction velocity, defined by equation 3.21, and y is the distance from the centre of the first layer of cells to the wall surface.

$$u_\tau = \sqrt{\frac{\tau_w}{\rho}} \quad 3.21$$

where τ_w is the local wall shear stress, defined by equation 3.22.

$$\tau_w \equiv \frac{1}{2} C_f \rho U_\infty^2 \quad 3.22$$

where U_∞ is the free-stream velocity and C_f is the skin friction coefficient, which for a turbulent boundary layer has many approximations. One such approximation with experimental calibration is the 1/7 power law given by equation 3.23 [36].

$$C_f = \frac{0.0592}{Re_x^{1/5}} \quad 3.23$$

A wall treatment is a set of modelling assumptions for the region near the wall which is used for a turbulence model which does not model this region sufficiently accurately. They comprise a set of functions to satisfy the physics of the flow in the region near the wall where four areas are identified: the laminar sub-layer, the buffer region, the log law region and the outer region. The wall functions are used to bridge this buffer layer, where neither the log law nor $u^+ = y^+$ are accurate.

The standard k- ϵ model does not account for viscous stress. It uses the log law equation only and so $y^+ > 11.6$ has to be obeyed for accurate results. The standard k- ϵ model with enhanced wall treatment uses the log law, equation 3.18, when $y^+ > 11.6$ and switches to the laminar viscous sub-layer equation when it detects $y^+ < 5$. Therefore, the buffer region, which is $5 < y^+ < 11.6$, is inaccurately modelled.

The k- ω model with low Reynolds corrections accounts for the viscous stress which makes it an accurate model for the laminar sub-layer, meaning y^+ has to be less than 5. However, it is not so accurate when modelling free-stream flow.

The SST k- ω model with low Reynolds corrections has the accurate property of the k- ω model for the laminar sub-layer when $y^+ < 5$ but switches to the standard k- ϵ model to give accurate modelling in the range $y^+ > 11.6$.

4 Methodologies

This section of the report discusses the methodologies used during the project.

4.1 Project management

Progress was reviewed at the weekly group meetings with Dr Gavin Tabor, Dr Matt Eames and Edward Shorthouse, when decisions were taken concerning the course of the project. Relevant theory topics were also discussed. The group members also had meetings later in each week to discuss and follow up the matters which had been raised in the supervised meeting.

Supervised meetings were chaired by each member of the group in rotation, the chairperson being the secretary from the meeting in the previous week so that the minutes were also taken by each group member in turn. The supervised minutes were reviewed in the next week's meeting to ensure that action points were followed up.

A Gantt chart was maintained in order to manage and plan the completion of the project objectives effectively. The chart in Figure 4.1 outlines the record of the tasks undertaken.

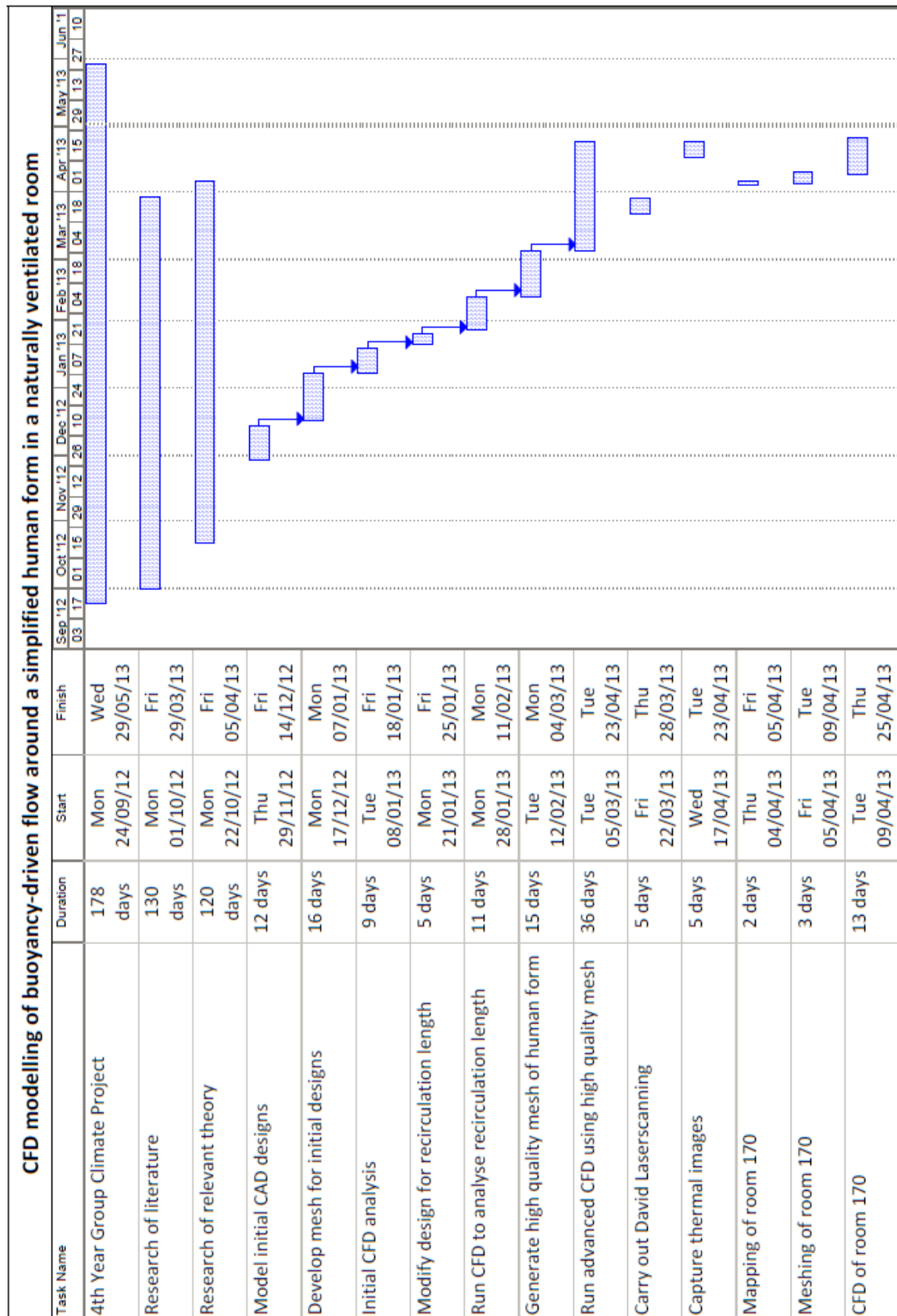


Figure 4.1: project Gantt chart

4.2 Literature research

The University Electronic Library gave access to the Compendex and EBSCO journal article services which were used as the main sources of literature for the survey.

4.3 Theory concepts

An initial guide to unfamiliar concepts was obtained from CFD Online and Wikipedia followed by reference to textbooks and discussions with the Dr Gavin Tabor in the weekly meetings.

4.4 Different geometry designs

All geometrical designs were made using SolidWorks as it has been the preferred design package taught throughout the degree course, apart from two cases where the geometry was downloaded from the GrabCAD 3D Library [37].

4.5 CFD in ANSYS

A user account was set up with the ANSYS Student Portal to enable access to tutorials and help pages, together with referral of specific problems to trained ANSYS Technicians to gain professional CFD help. Another main reason for using the portal was to view tutorials with step-by-step instruction of how to carry out specific procedures. Additional CFD help was also obtained via the CFD Online forum.

4.6 David Laserscanner

The David Laserscanner technique was used to scan the surface of a Manikin in order to create 3D geometry, with the original intention of going on to scan full size human body. A 5mW eye-safe line-laser and a webcam were purchased, and software was downloaded through the David Laserscanner website. A risk assessment was carried out for the use of the laser, and can be found in Appendix B.

However, due to the limited power of the laser which made scanning of an object taller than the Manikin not possible, and the limited license for the free version of the software downloaded, complete 3D scans could not be saved for further use. Several screenshots were recorded while using the software and are shown in Appendix C.

4.7 Thermal imaging camera

A thermal imaging camera was borrowed from the Physics department in order to produce input data for the temperatures of the human surface, or to confirm the temperatures used from the literature research. However, as this part of the group project only dealt with a single-surface human geometry, and did not divide up the human into sections to input multiple temperatures, this data could only be used for this project as an illustration of the surface temperatures.

Images have not been included because they only show radiated heat energy and not the conduction which produces the convection because of buoyancy, which is the subject of this study.

4.8 Interlinking with the other sub-groups

The sensor sub-group provided temperature and air exchange rate data which was used in this section of the project as input boundary conditions for the CFD simulations. The modelling of Harrison lecture room 170 was carried out in order to provide comparisons with the results obtained by the room sub-group. The results from the modelling in this report which are based on an average surface temperature for the whole human form can be compared with the results from the model of the segmented human form, carried out in the other half of this sub-group, which used different surface temperatures for defined regions of the body. This is regarded as having potential for rapid scaling up of the numbers of persons in a room, in particular when the total buoyancy driving force is required to gauge the effectiveness of natural convection, especially in rooms without windows.

5 Design

5.1 Human forms

The designs modelled and considered in the project are shown in Figure 5.1 to Figure 5.5 in increasing level of complexity.

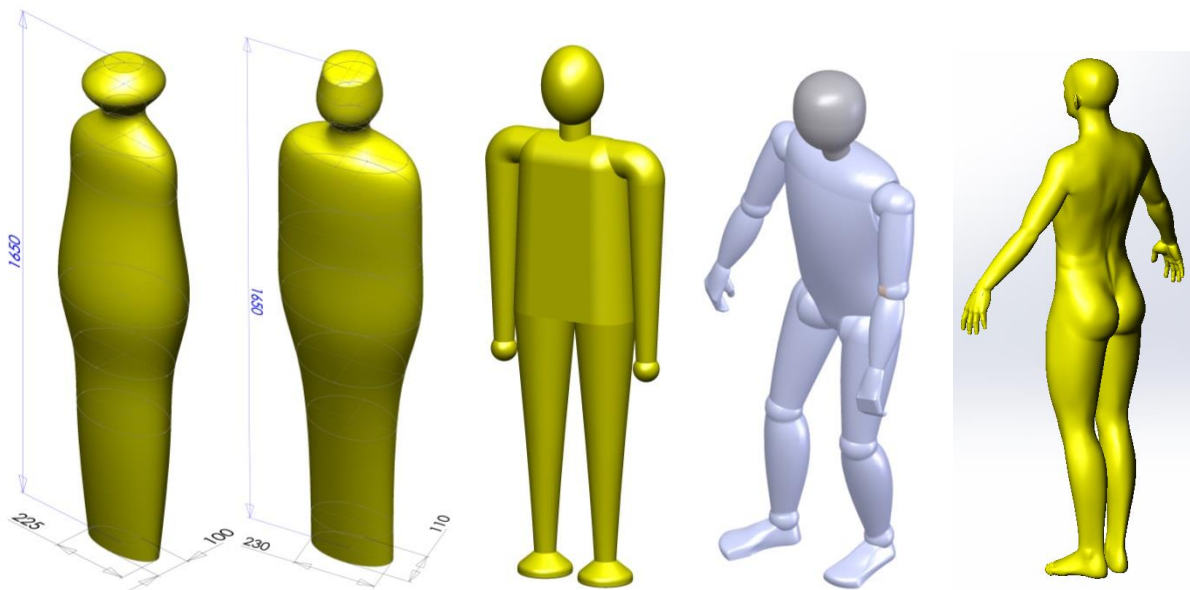


Figure 5.1:
initial design

Figure 5.2:
human form

Figure 5.3:
basic Manikin

Figure 5.4:
detailed Manikin

Figure 5.5:
human scan

5.1.1 Cylinder

It was considered that the simulation of a cylinder would be an appropriate place to start. This is because the cylinder in cross-flow is a classic example which has been used for teaching of concepts such as the von Karman street effect, the boundary layer separation angle and growth, and would be an appropriate first approximation to the human form. However, it was decided that this design was too limited for the investigation required, so little CFD was carried out using this geometry.

5.1.2 Initial design

The first simplified human design, Figure 5.1, resulted from research which suggested that an approximation of the human form could be readily produced by a loft consisting of a set of ellipses so that it was a continuous shape, without arms [13]. The importance of designing a surface which was developed without discontinuities or edges was relevant to the need for a relatively simple CFD mesh.

This was the preliminary meshing geometry, which was made in order to model the flow from a front inlet flowing over the surface of the human, in order to investigate the behaviour in the wake of the human for driven flow. Its main purpose proved to be the justification of the mesh created using ANSYS because the direction of the project moved to buoyancy-driven flow.

5.1.3 Human form

The initial concept led to the modification of the ellipse based loft to a more accurate approximation of the human form, with an increased number of ellipse profiles, shown by Figure 5.2. This still had no distinct limbs and is in a standing position, but for the reasons discussed in section 7, this was regarded as a reasonable approximation for the CFD carried out.

5.1.4 Basic Manikin

The first model actually designed by the human sub-group, Figure 5.3, was segmented in order to go on to set different surface temperatures to the various regions of the body to link in with work carried out using the Fiala comfort model. However, there were concerns about the difficulty in creating the mesh for this relatively complicated structure in view of the importance of modelling the boundary layer in buoyancy-driven flow. This led to the decision to pursue the research on two fronts; in this section the creation of an accurate mesh was given priority over sophistication of the model from a human comfort aspect.

5.1.5 Detailed Manikin

A Manikin SolidWorks model was downloaded from GrabCAD [37] with the intent of using it for more accurate CFD of the flow around a human, Figure 5.4. Apart from requiring some modification to the model to align the feet, the Manikin was ready for use in ANSYS. The design was placed inside a control volume to enable CFD, and a mesh was created, using default settings in ANSYS.

5.1.6 Human scan

Finally, the latest and most sophisticated CTM geometry can be obtained by use of the laser scanning technique, and in this project the David Laserscanner technique was used. This involves scanning a three-dimensional object using a line laser and a camera. All the fine geometry characteristics and extremities of the human body can be represented by using this technique [9] [7]. The image is digitalised and can easily be imported into SolidWorks.

In addition, a full and accurate human scan was downloaded from GrabCAD, Figure 5.5, although it was a surface-body rather than a solid-body. This is included for reference purposes for future work.

However, both of these scanned models will require a mesh of much higher resolution and are likely therefore to significantly increase the simulation time.

5.2 Integration with room 170 model

The 3D lecture theatre, room 170 in Harrison building, was identified by the group as a suitable room for experimental and computational research and therefore it was modelled as shown in Figure 5.6.

Room 170 does not have symmetry in the configuration of the inlets, outlets and lights in the ceiling. This meant that it was not possible to have a section plane down the steps of the lecture theatre in order to halve the size of the mesh by dividing it into an exact mirrored half, without deviating from reality. If it had been possible it would have been more economical in the solving time.

In model room 170 the bench configuration was blocked in to decrease computational time. The loss of accuracy was considered to be minimal because of the proximity of the desk work surfaces and the seats. The computer and the doors to the room were also not modelled because it was believed that these would not significantly change the flow behaviour in the room, as the temperature of both was close to the normal wall temperature.

The ceiling tiles, which were measured at the back of the theatre for ease, are of uniform size 57x57cm apart from the strips nearest to the wall at the projector and screen sides of the room, where the tile size was 47x57cm. There is a uniform gap of 3cm around all tiles. This provided an accurate grid for the mapping of the ceiling and its inlet vents, outlets and light fittings which were all located in the place of a normal tile. The large square vents are the inlets, the smaller square vents are the outlets and the rectangular shapes are the lights.

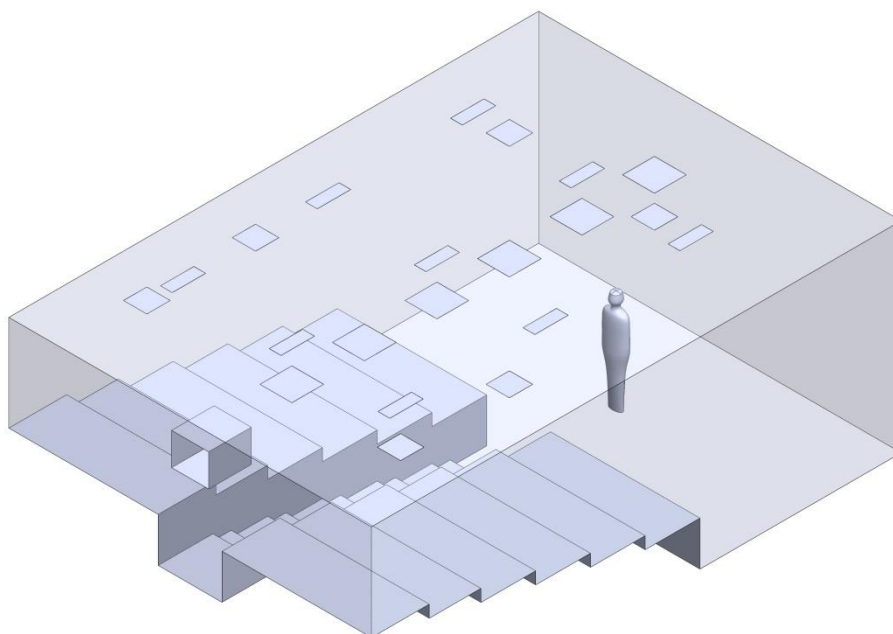


Figure 5.6: Harrison room 170 inverted model with human form

6 CFD

CFD is a technique for modelling the flow of a fluid by dividing the whole volume of the fluid into small volumes or cells so that the Navier-Stokes equations can be solved numerically for the central points of the cells using an iterative process.

In this study the human geometries were encased by a control volume and then the volume representing the human was subtracted in order to leave a solid volume that would represent the air around the human. It is important to note that the geometry needed to be a single body part. The inverted geometry was then exported directly to ANSYS using the built-in SolidWorks function, as this CAD import strategy had been tried and tested in previous projects and was found to be the most efficient method. This method was used throughout the project.

Designing the human in ANSYS itself was considered, but due to the advanced tools and familiarity with SolidWorks, that approach was chosen over ANSYS.

Named selections were used throughout the project as the method for controlling the selection of surfaces in order to define local mesh settings along with boundary conditions for particular faces or collections of faces.

Mesh refinement studies were carried out in order to determine when the maximum velocity in the domain had reached an accurate value and had stopped changing value, to minimise the size of the mesh and therefore the time taken to solve the simulation. However, the results did not show clear convergence at any particular number of cells, therefore upper values were chosen because of the computational power available.

6.1 Initial CFD

The aim of this section of the CFD was to position the initial design of Figure 5.1 in a control volume in the form of a cube of 2m, in order to model driven airflow. The initial setup was with driven flow from a side wall, as in the combination of wind and natural convection, representing a situation such as an open window.

A series of meshes was created in the process of generating a mesh of sufficiently high quality. Both global maximum and minimum cell sizes were specified and then specific controls were set for particular surfaces, these controls being size limitations and inflation control for the boundary layer. The transition of cell size from just outside the boundary layer mesh to the external walls was set to slow to keep the grid resolution high close to the human. The thickness of the inflation mesh required to accurately resolve the boundary layer was calculated using equation 3.16. The settings for the optimum mesh are summarised in Table 6.1.

Table 6.1: optimum mesh settings

Global Size [mm]		Inflation settings			Human surface cell size [mm]
Min.	Max.	Layers	Max. thickness [mm]	Rate	
2	32	7	18	1.1	3

After each mesh was created, the statistics of the mesh produced were used to analyse its quality, which was also assessed by looking at a cross-section of the control volume. These statistics for the final (optimum) mesh are shown in Table 6.2.

Table 6.2: optimum mesh statistics

Number of cells	Average cell quality	Average skewness
2,592,465	0.949	0.105

Figure 6.1 (left) shows the mesh using the optimal settings, whilst Figure 6.1 (right) shows a close-up view of the boundary layer of this mesh.

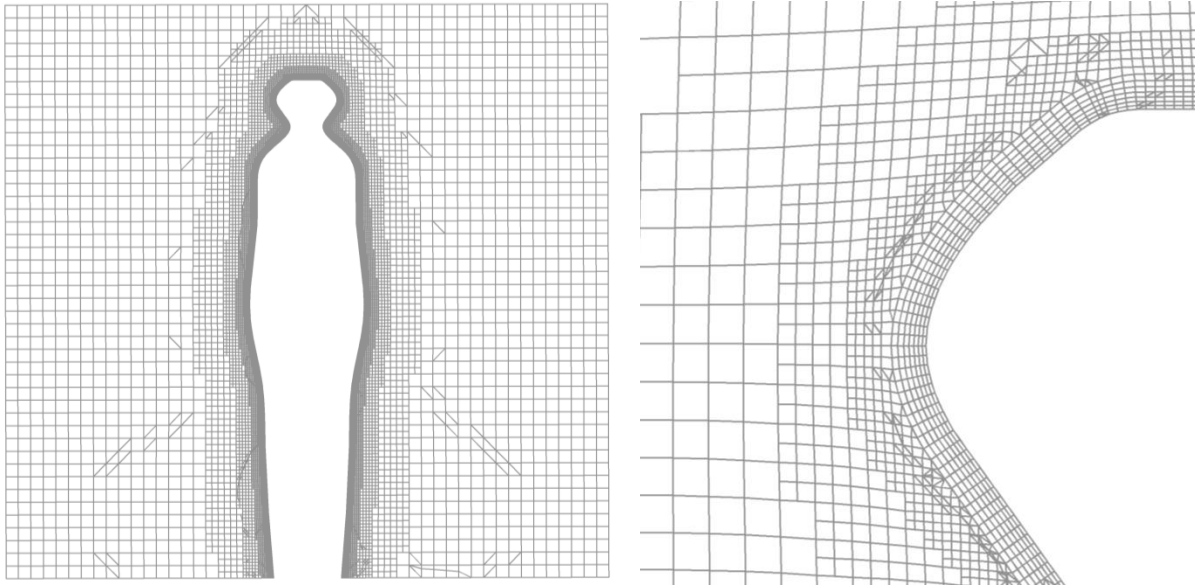


Figure 6.1: initial design meshed using the settings in Table 6.1 (left), close-up view of the boundary layer mesh (right)

An initial simulation was carried out to check the results produced for the mesh, as shown by Figure 6.2. It is evident that the domain did not have enough space behind the human to adequately model the fluid recirculation. Therefore, the space behind the human was extended so that the overall length of the domain was 3.5m, with an increase in the height of the domain to 2.15m, to give a head room of 0.5m. Due to the increased size of the domain, it was necessary to halve it down its length in order to produce a mesh of the same resolution and still have the computational power to be able to be meshed and solved.

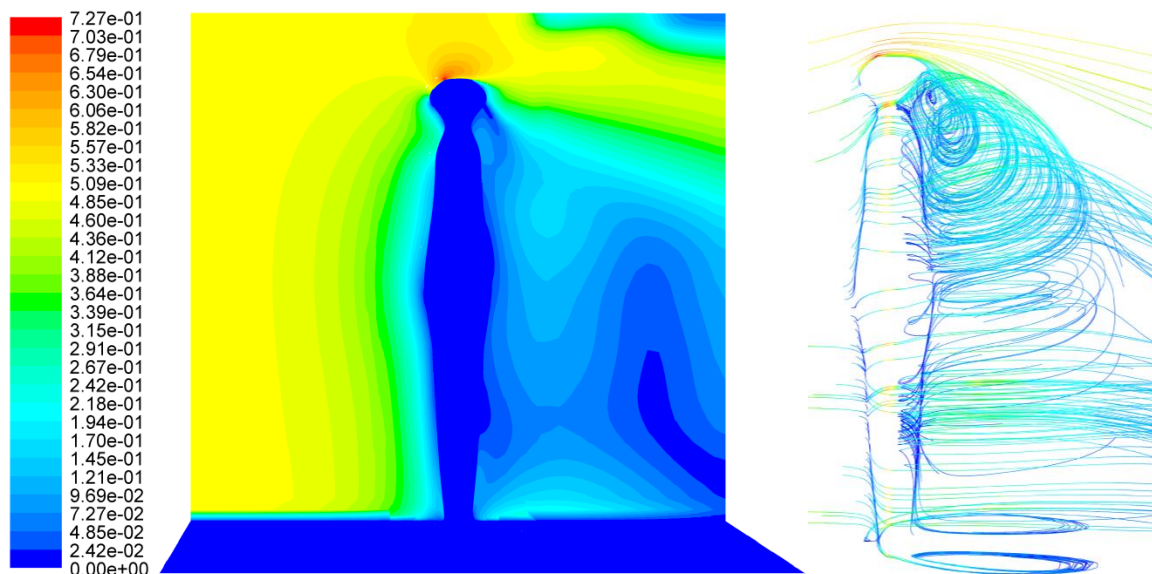


Figure 6.2: contours of velocity mag. [ms^{-1}] for the initial CFD (left), pathlines coloured by velocity mag. [ms^{-1}] (right)

In a separate case, because of the complexity of purely buoyancy-induced flow and of modelling it accurately, the floor surface was also set up to be an inlet at low velocity in order to kick-start the model, which is sometimes necessary in models where buoyancy produces the flow. However, this was not found to be necessary, as the buoyancy effect induced the flow and so this approach was not pursued.

The results from this increased length showed that the recirculation zone was properly modelled. However, the course of the project progressed to purely buoyancy-driven flow. The setup established in this section was applied in creating suitable meshes in the following sections.

6.2 Human form

The main CFD modelling was carried out on the developed ellipse-based design of Figure 5.2 in order to more accurately represent the core outline of the human, without clearly delineated or defined limbs.

Most of the CFD research was carried out on the refined ellipse loft model, investigating natural convection resulting from buoyancy-driven flow.

As before, a control volume around the human was made, which was then halved to reduce the mesh size and therefore solving time. Two inlet surfaces at the base and a single outlet surface at the top, all of size $250 \times 250 \text{ mm}$, were included by extruding a square cut into the solid by a negligible distance of 0.001 mm .

6.2.1 Mesh generation

Due to the increased processing power available from the use of the high-powered Linux-based computers, the set-up of which is described in section 10.1, much larger meshes were possible from this point onward. The meshing method established in the previous section was applied for the control volume around the improved human form design. The settings used previously, in Table 6.1, were modified in order to produce a mesh that had the correct cell size in the boundary layer in accordance with the wall value requirement. The mesh settings used for the mesh produced are given in Table 6.3.

Table 6.3: mesh settings for human form

Global Size [mm]		Inflation settings			Human surface cell size [mm]
Min.	Max.	Layers	Max. thickness [mm]	Rate	
2	16	10	18	1.1	3

As shown by Table 6.4, the statistics for the refined mesh show that it is of sufficiently high quality.

Table 6.4: mesh statistics for human form

Number of cells	Average cell quality	Average skewness
6,673,897	0.960	0.048

Figure 6.3 illustrates the mesh around the head of the human form.

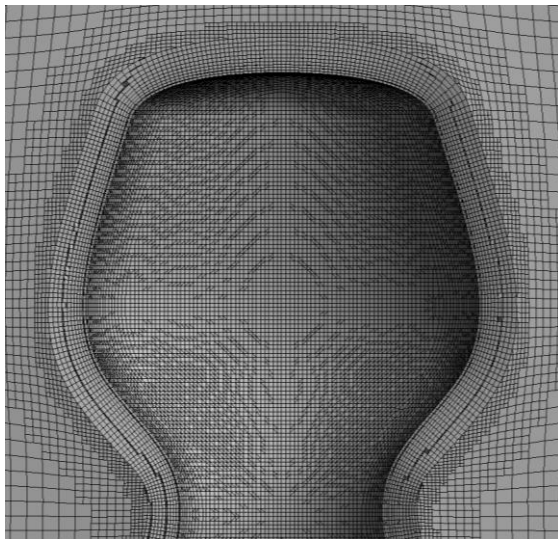


Figure 6.3: mesh for the head of the human form

6.2.2 Fluent set-up

A steady-state simulation in Fluent was set up in ANSYS with the gravity setting enabled. The energy equation was enabled and the turbulence model was chosen. The air properties used were those given in Table 6.5 [38]. Of particular importance was the selection of the air density model which was set to Boussinesq, which enables the Boussinesq approximation discussed in section 3.2.

Table 6.5: properties of air [38]

Temperature T [K]	Density ρ [kgm ⁻³]	Dynamic viscosity μ [m ² s ⁻¹]	Specific heat capacity c_p [Jkg ⁻¹ K ⁻¹]	Thermal conductivity k [Wm ⁻¹ K ⁻¹]	Thermal diffusivity α [m ² s ⁻¹]	Expansion coefficient β [K ⁻¹]
293	1.205	1.511E-05	1005	0.0257	2.12E-05	0.00343

Three cases of the temperature difference between the surface of the human and the surrounding walls, ΔT , were considered in this CFD to show the effect for three average human surface temperatures. The Rayleigh and Grashof dimensionless groups discussed in section 3.1 were calculated for two different points up the length of the human, Figure 6.8, taking the base of the human as zero.

The Rayleigh number at the waist height of 0.8m indicates that the heat transfer is mainly in the form of convection, whilst at the head height of 1.65m the heat transfer is almost entirely in the form of convection.

The Grashof numbers calculated for both heights and all temperature differences indicate that the flow is in the transition stage between laminar and turbulent flow and can therefore be considered to be turbulent.

Table 6.6: calculated values of the dimensionless groups

Length scale L [m]	ΔT [K]	Rayleigh Ra []	Grashof Gr []
0.80	5	2.69E+08	3.77E+08
0.80	9	4.84E+08	6.79E+08
0.80	13	6.98E+08	9.81E+08
1.65	5	2.36E+09	3.31E+09
1.65	9	4.24E+09	5.96E+09
1.65	13	6.13E+09	8.61E+09

Next, the boundary conditions were defined. The choice of the temperatures of the walls was based on the research, summarised in Table 6.7.

Table 6.7: boundary conditions used in simulations

Location	Type	Temperature [K]
Human surface	Wall	298, 302, 306
Inlet	Inlet-vent	293
Outlet	Outlet-vent	293
Walls	Wall	293
Symmetry wall	Symmetry	293

Some of the simulations failed to converge to the desired accuracy that all residuals be lower than 0.0005. Under-relaxation factors limit the influence of the previous iteration over the present one as they control the blending (how much is blended from the last run to the current run). In cases where a simulation would have difficulty solving, the factors were lowered by up to 0.2 to help the convergence. Reducing these factors may also prevent oscillations in the residuals developing, but with the consequence that the solution may need longer to converge. By default, ANSYS Fluent uses an under-relaxation factor of 1.0 for the energy equation. In cases where the energy field impacts the fluid flow, via temperature dependent properties or buoyancy, it is recommended that a lower value should be used, in the range 0.8-1.0 [39].

6.2.3 Results

The turbulence models used in this section were the standard k- ϵ model with enhanced wall treatment and the SST k- ω model. The three different temperature differences were modelled for each turbulence model, as summarised in Table 6.8. The induced mass flow rate at the inlets was recorded, along with the heat transfer between the energy of the outlet when compared to the inlet.

Table 6.8: results for human form simulations

	Turbulence model	ΔT [K]	Induced mass flow rate [$g s^{-1}$]	Heat transfer between inlets and outlet [W]
Run 1	Std k- ϵ	5.0	9.6	3.81
Run 2	Std k- ϵ	9.0	13.2	9.81
Run 3	Std k- ϵ	13.0	12.9	10.08
Run 4	SST k- ω	5.0	9.5	4.54
Run 5	SST k- ω	9.0	14.0	13.99
Run 6	SST k- ω	13.0	15.8	20.97

The results in Run 3 appear to be an anomaly, and the simulation was re-run from the beginning with a similar set of results. This led to the conclusion that the induced flow rate for Run 3 may not have increased because the increased buoyancy force resulted in turbulence in the control volume, or that it was merely an inaccuracy relating to the setup.

The velocity magnitude contour plot in Figure 6.4 for the standard k- ϵ model shows symmetry indicating a mesh of high quality. It also compares with the equivalent plot for the SST k- ω model, however, that model does not show such good symmetry.

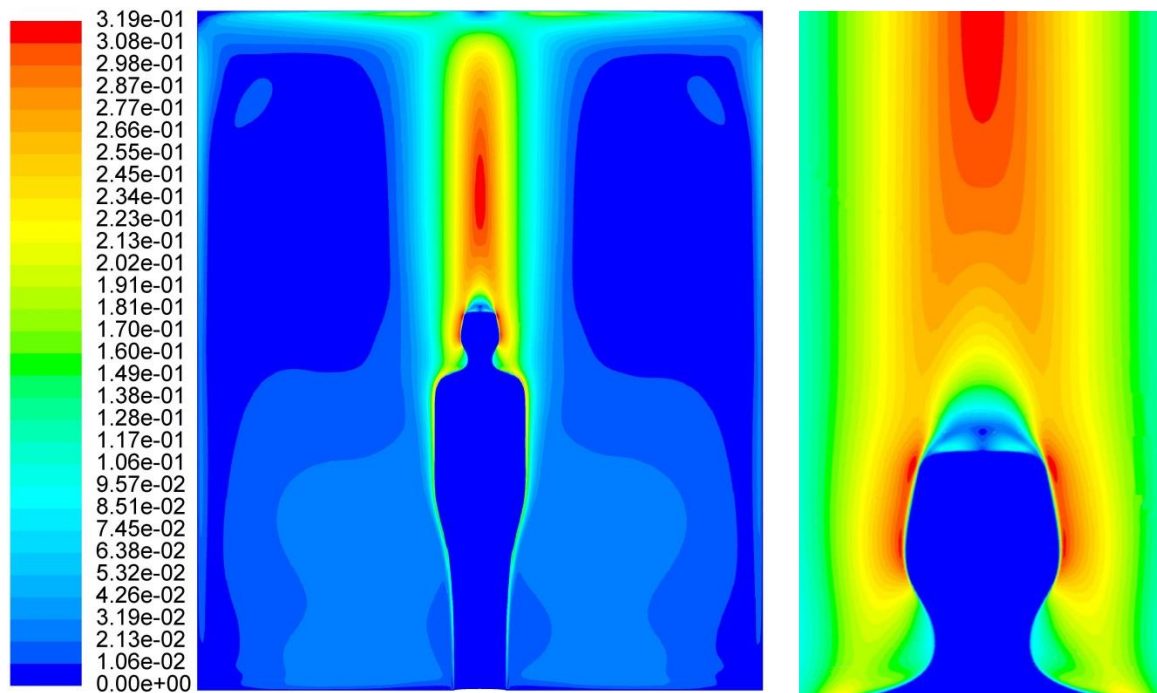


Figure 6.4: contours of velocity mag. $[\text{ms}^{-1}]$ for Run 2 at the symmetry plane (left), close-up view of head (right)

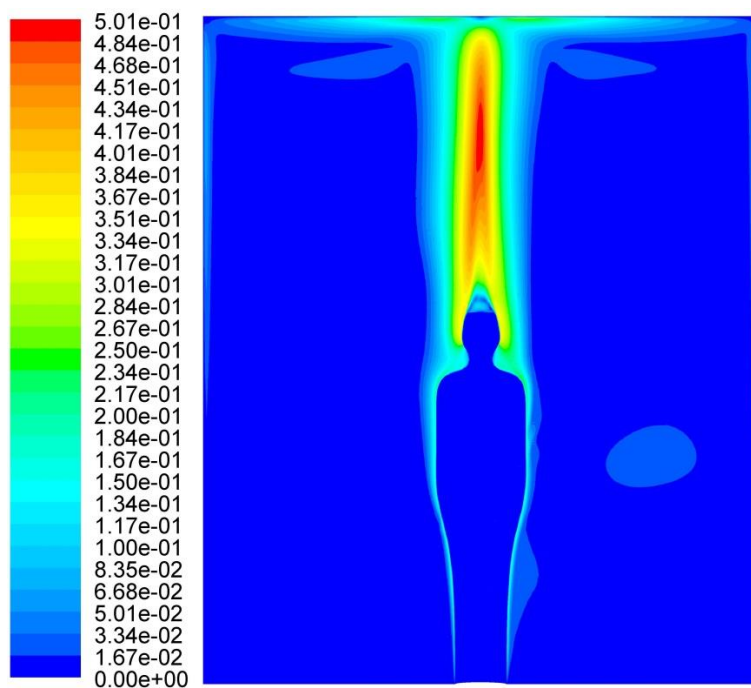


Figure 6.5: contours of velocity mag. $[\text{ms}^{-1}]$ for Run 5 at the symmetry plane

Figure 6.6 shows a contour plot coloured by velocity magnitude at the inlet/outlet section plane for the standard $k-\epsilon$ model. As before, there is clear symmetry with air being sucked in through the inlets and pushed out via the outlets.

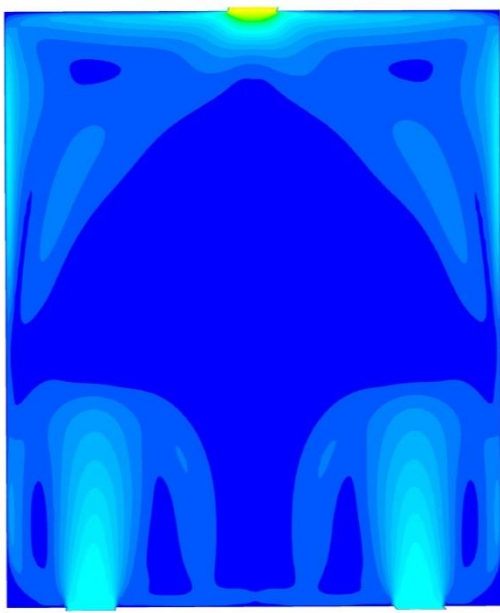


Figure 6.6: contours of velocity mag. [ms^{-1}] for Run 2 at inlet/outlet plane

The total temperature contour plot in Figure 6.7 shows a thermal plume rising from the human and the effect this has on the top of the control volume, using the standard $k-\epsilon$ model. It compares well with the equivalent plot for the SST $k-\omega$ model in Figure 6.8. On both temperature plots it is noticeable that the plume narrows to form a jet-like shape.

The results show that this simplification of representation of a human form produced a similar thermal plume to that generated in the more accurate human shape in Figure 2.2 from the literature review.

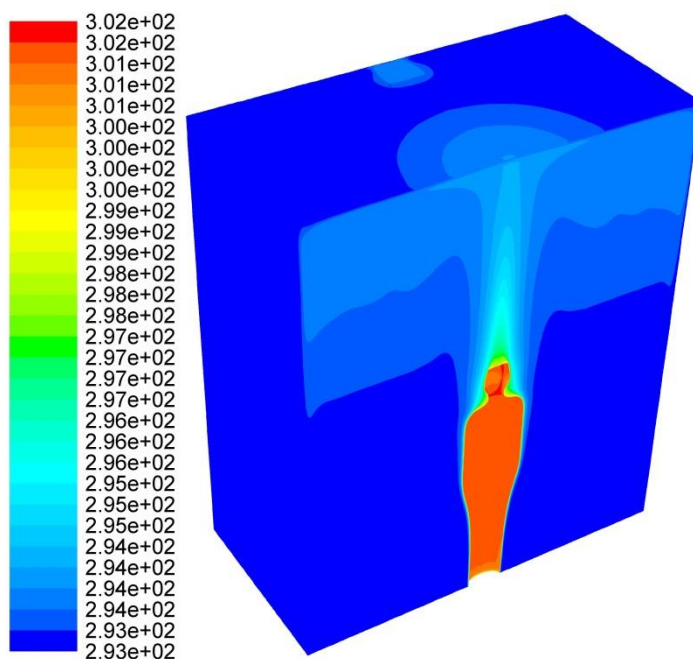


Figure 6.7: contours of total temperature [K] for Run 2

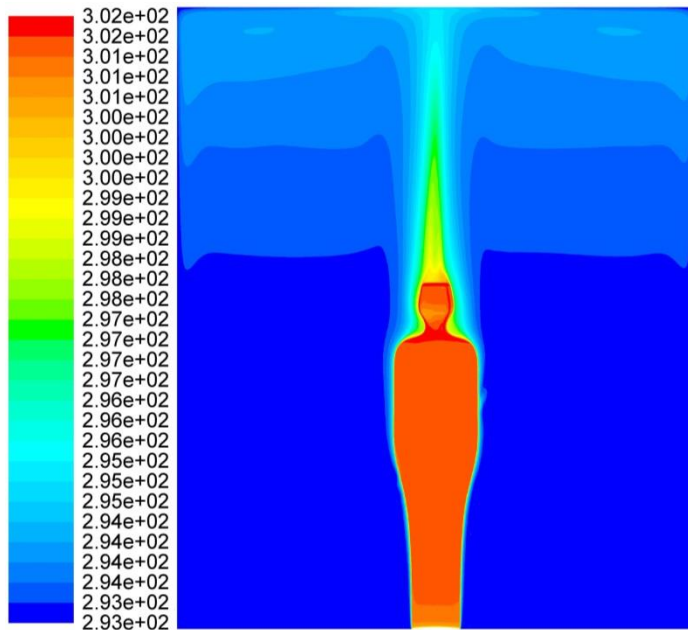


Figure 6.8: contours of total temperature [K] for Run 5

Figure 6.9 and Figure 6.10 show histograms of the wall y^+ values as a percentage of the surface cells for Run 2 and Run 5, respectively. They have comparative sizes and both fulfil the requirement that $y^+ < 2$, apart from a very low percentage where cells fall slightly above this value.

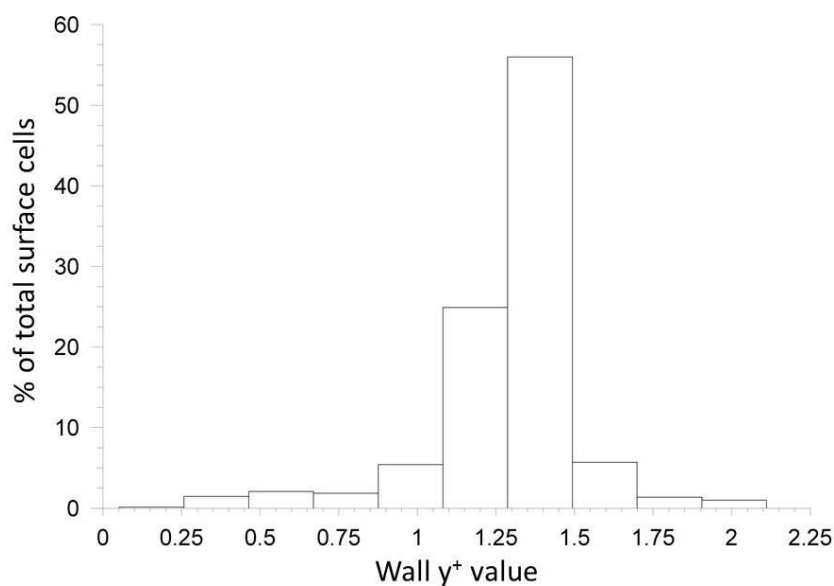


Figure 6.9: histogram of wall y^+ values for Run 2

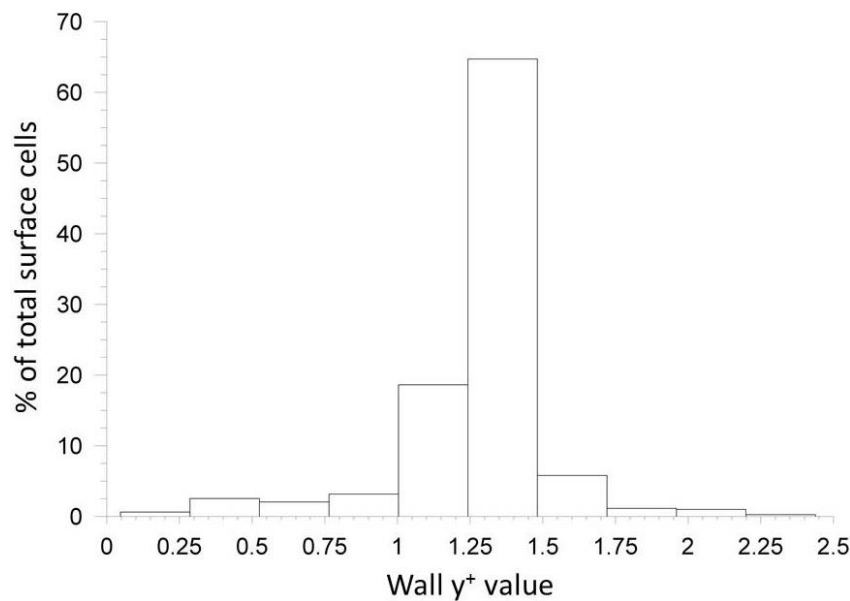


Figure 6.10: histogram of wall y^+ values for Run 5

6.3 Harrison room 170

The human form of Figure 5.2 was placed inside the room geometry in order to give the geometry of Figure 5.6. It was then inverted to give the air present in the room, using the same method as before.

Due to the asymmetry nature of room 170 (the tile system causing the inlets, outlets and lights to not be symmetrical along the length of the room), it was not possible to halve it in order to halve the mesh size and reduce computation time, or enable a higher resolution mesh. In order for the room model to be realistic, it was decided that forcing the inlets and outlets to be symmetrical would not be ideal. Future work could use a room model which did have symmetric ceiling panels, and so attain a higher resolution mesh, or alternatively enable modelling of more than one human.

Experimental data was recorded by the sensor group using a tracer gas to determine the average air exchange rate which when combined with the volume of the room and the total area of the inlet vents gave the velocity required for the inlets, as shown in Table 6.9.

Table 6.9: room 170 inlet velocity calculation

Volume of SolidWorks room 170 model [m³]	135.52
Air exchange rate [s⁻¹]	0.001415
Air volumetric flow rate [m³s⁻¹]	0.192
Area of 6 inlet vents [m²]	1.647
Air inlet velocity [ms⁻¹]	0.116

6.3.1 Mesh creation

The boundary layer mesh settings used for the human form in the control volume were applied to the human in the room. The inlets and outlets of the room 170 model had sizing limitations placed on them to force them to be of a certain size, as highlighted by Figure 6.11. As with the previous case, global maximum and minimum cell sizes were used. A summary of the settings used is given by Table 6.10, and the statistics for the mesh produced in are shown in Table 6.11.

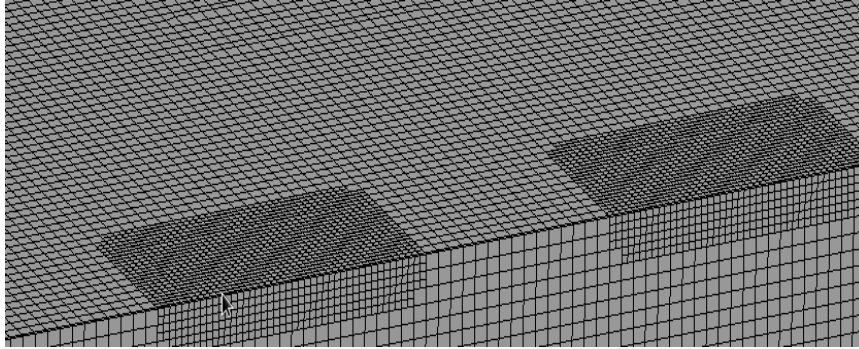


Figure 6.11: cross-section view of the mesh at the inlet vents

Table 6.10: mesh settings for room 170

Global Size [mm]		Inflation settings			Human surface cell size [mm]	Inlet/outlet cell size [mm]
Min.	Max.	Layers	Max. thickness [mm]	Rate		
1	32	10	18	1.1	3	16

Table 6.11: mesh statistics for room 170

Number of cells	Average cell quality	Average skewness
10,007,801	0.946	0.063

6.3.2 Fluent set-up

The core settings used for the human form case were also applied in this section. The assumed boundary conditions used in section 6.2 were supported by the experimental data taken by the sensor sub-group as shown in Table 6.12. In reality, the projectors used fans to maintain their operating temperatures, which resulted in the sucking in of air from the room and the emission of heated air. Therefore the projector acts as an additional set of inlet and outlet boundary conditions which were not modelled due to the additional complexity this would have imposed.

Table 6.12: room 170 temperatures recorded by the sensor sub-group

Location	Temperature readings [°C]				
	1st	2nd	3rd	4th	Average
Main Door	20.5	20.8	20.3	20.1	20.4
Front wall	20.2	20.6	20.3	20.0	20.3
Small door	20.3	20.5	20.2	20.1	20.3
Computer	20.2	20.6	20.3	20.0	20.3
Back wall	21.0	21.1	20.5	20.0	20.7
Projector	42.5	44.3	42.9	43.6	43.3
Inlet vents	16.0	16.2	16.1	16.0	16.1
Ceiling	20.9	21.3	20.7	20.2	20.8
Lights	20.8	21.2	20.6	20.2	20.7

6.3.3 Results

Two main simulations were carried out for the room model, the first used the standard k- ϵ model with enhanced wall treatment and the second the SST k- ω model. However, due to problems in the solving of the second, the results of this are not shown. Figure 6.12 shows contours of velocity magnitude of the bisecting plane of inlet vents illustrating the inlet jets, with the human form in front of this plane.

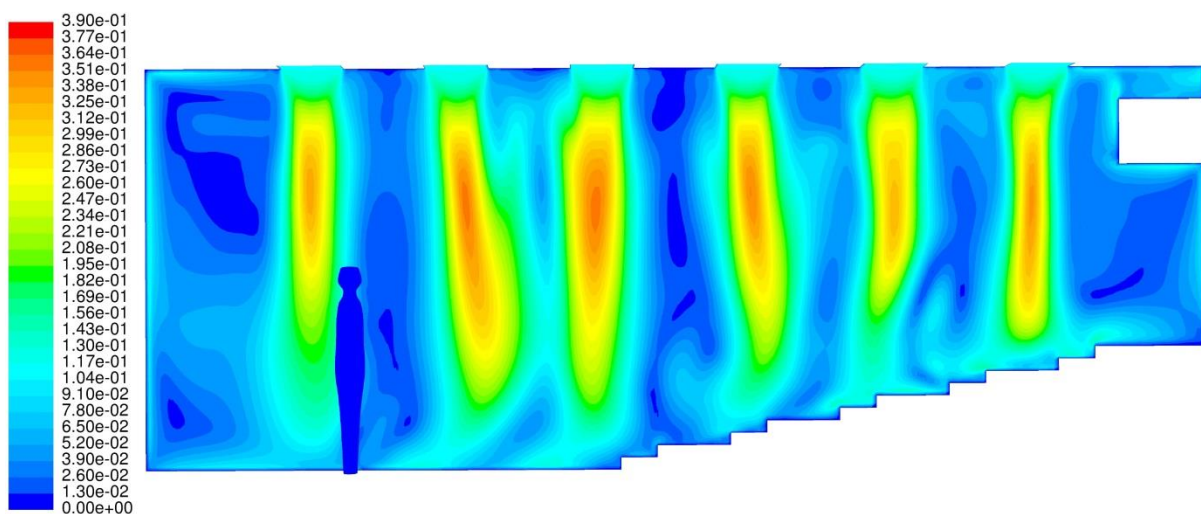
Figure 6.12: contours of velocity mag. [ms^{-1}] for standard k- ϵ model at inlet plane

Figure 6.13 is a similar plot but using the plane that bisects the human and therefore the centre of the room. It is noticeable that the inlet vents are mostly out of view, which indicates that the jets remain concentrated vertically.

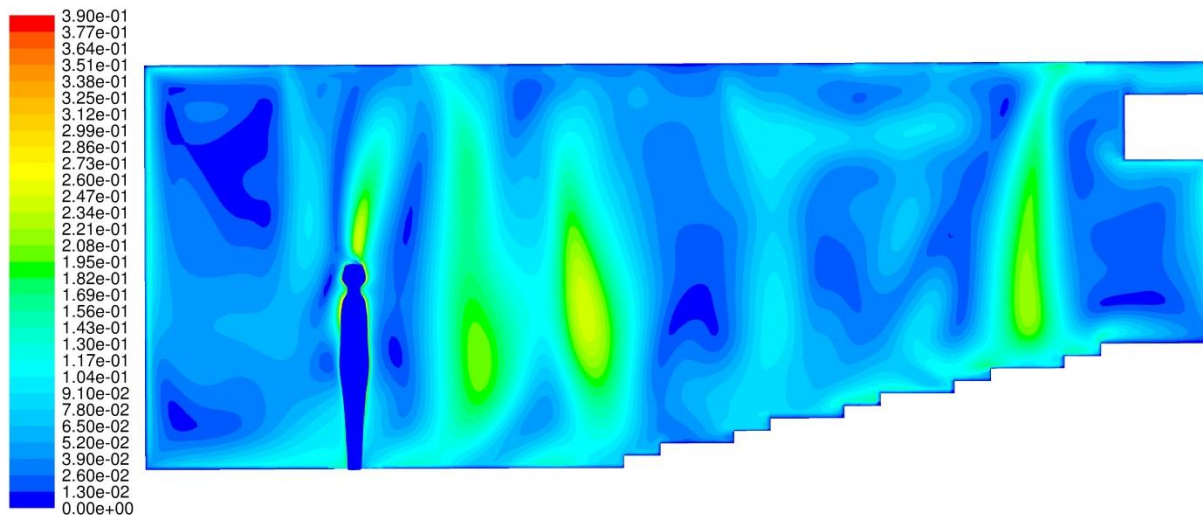


Figure 6.13: contours of velocity mag. [ms^{-1}] for standard k- ϵ model at human plane

Figure 6.14 shows contours of total temperature for the inlet bisecting plane, highlighting the cooler air entering the room from the inlet ducts and the effect the heated projector has on the air above it.

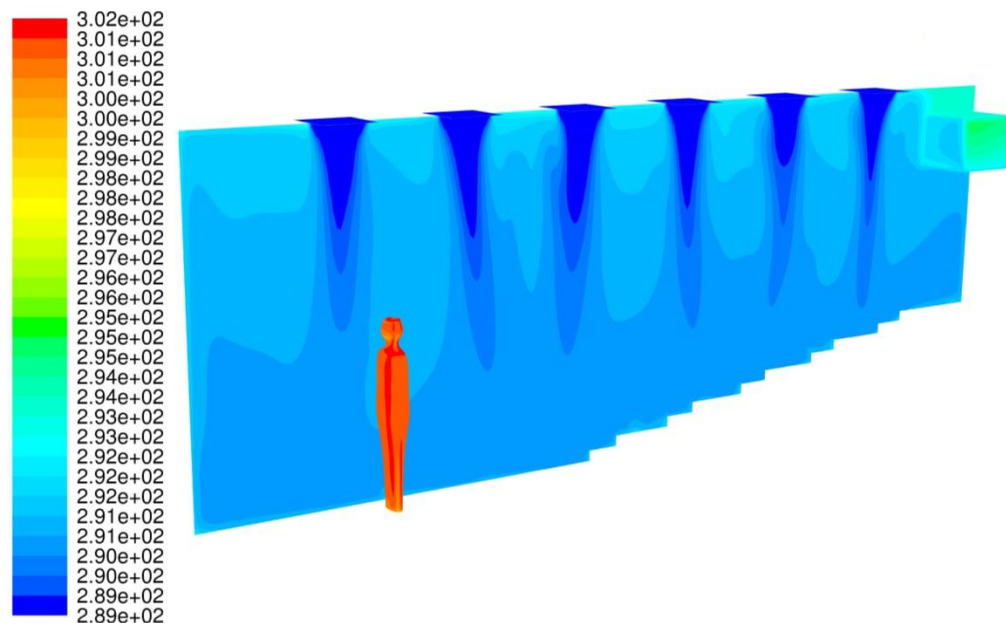


Figure 6.14: contours of total temperature [K] for standard k- ϵ model at inlet plane

6.4 Sources of error

In running CFD computations, a single mesh cell could prevent convergence by being of poor quality, hence the need for care in mesh design. The shape of the cells in a mesh is fundamental, which is where mesh statistics such as cell quality, skewness and aspect ratio play an important role in confirming that the mesh is satisfactory.

The selection of the appropriate turbulence model is particularly important because of the turbulent flow in the boundary layer in this project. Different models use different equations and therefore the results produced are likely not to be the same, as seen in the results of section 6.2. Input parameters such as the inlet turbulent intensity and length scale also affect the results produced.

7 Analysis and discussion

The main technical problem in this project concerned defining the mesh to simulate the flow around the human form. Consequently, the modelling of the segmented human form was not pursued so that modelling could be conducted on a single surface human. This had the advantage of simplifying the mesh and ensuring that the modelling of this simplified design of the human form would readily solve. This is considered to be a valid approach as an alternative to the research on the human comfort model. This is because there are two main aspects of natural ventilation systems: the comfort of the human individual and the buoyancy force driving the system.

Since people rarely sit still, it was considered that modelling the average effect of a single surface human form would be a justified alternative approach. The research in this project is based on a human form without distinct arms and legs, therefore being based on a core shape which lends itself to scaling up for numbers of people and disregarding their specific location, and to some extent their movement around the office. Whereas the flow around a seated human is important from the human comfort point of view, the movement both of limbs and of the human within a room will disturb the flow and so the averaging effect of using a single surface may not be significant.

Future research might include the effect on the plume, and hence the natural convection, of the movement of a human within the office environment. There are two aspects to this: the first is that in order to obtain reliable data on the natural convection, the average effect of an average size human being has to be established; and the second is how much of a difference the inclusion of limbs and their alignment with the body makes to the plume and the natural convection.

8 Conclusions

Given the variation in human body forms (shapes and sizes), the variable numbers of people in a room, their attitude (position of arms in relation to body), and whether they are in motion or not, there would seem to be significant value in modelling a simplified human form for this area of research. The size of this simplified form could be readily changed for comparative testing or modelling. Further work could be carried out on testing the hypothesis that this idealised human form produces results similar to those for a detailed human shape, and assessing the level of inaccuracy. If the occupants of a room are to be used to drive the flow in a naturally ventilated room, it will be important to assess the effect of varying numbers of them.

The work undertaken in this report provided significant experience in more advanced modelling and established procedures for incorporated this project into the related group work. Future work could include the following:

- The effect of different inlet velocities and their comparison
- The effect of different inlet temperatures and human surface temperatures
- Modification of the room geometry to half the volume and so mesh size, to enable multiple human models to represent sitting in the seats
- Use of more detailed human geometry for the CFD analysis

9 References

- [1] J. Imbrie and P. K. Imbrie, *Ices Ages: Solving the Mystery*, Harvard University Press, 1979.
- [2] P. de Wilde and W. Tian, "Predicting the performance of an office under climate change: A study of metrics, sensitivity and zonal resolution," *Energy and Buildings*, vol. 42, pp. 1674-1684, 2010.
- [3] T. Catalina, J. Virgone and F. Kuznik, "Evaluation of thermal comfort using combine CFD and experimentation study in a test room equipped with a cooling ceiling," *Building and Environment*, vol. 44, pp. 1740-1750, 2009.
- [4] A. Roetzel and A. Tsangrassoullis, "Impact of climate change on comfort and energy performance in offices," *Building and Environment*, vol. 57, pp. 349-361, 2012.
- [5] M. J. Cook and J. L. Lomas, "Guidance on the use of computational fluid dynamics for modelling buoyancy driven flows," Institute of Energy & Sustainable Development, De Montfort University, Leicester, 1997.
- [6] P. F. Linden, G. F. Lane-Serff and D. A. Smeed, "Emptying Filling Boxes: The Fluid Mechanics of Natural Ventilation," *Journal of Fluid Mechanics*, vol. 212, pp. 309-335, 1990.
- [7] N. P. Gao and J. L. Niu, "CFD Study of the Thermal Environment around a Human Body: A Review," *Indoor and Built Environment*, vol. 14, pp. 5-16, 2005.
- [8] P. C. Cropper, T. Yang, M. J. Cook, D. Fiala and R. Yousaf, "Coupling a model of human thermoregulation with computational fluid dynamics for predicting human-environment interaction," Leicester University, Leicester, 2009.
- [9] N. Gao and J. Niu, "CFD study on micro-environment around human body and personalized ventilation," *Building and Environment*, vol. 39, pp. 795-805, 2004.
- [10] J. A. J. Stolwijk, "A mathematical model of physiological temperature regulation in man," NASA, Washington, 1971.
- [11] H. O. Nilsson, "Thermal comfort evaluation with virtual manikin methods," *Building and Environment*, vol. 42, pp. 4000-4005, 2007.
- [12] S. J. Dunnett, "A numerical study of the factors affecting worker exposure to contaminant," *Journal of Aerosol Science*, vol. 25, pp. 481-482, 1994.
- [13] S. Murakami, J. Zeng and T. Hayashi, "CFD analysis of wind environment around a human body," *Journal of Wind Engineering and Industrial Aerodynamics*, vol. 83, pp. 393-408, 1999.
- [14] CFD Online, "K-omega models," 2013. [Online]. Available: http://www.cfd-online.com/Wiki/K-omega_models.
- [15] CFD Online, "SST k-omega model," 2013. [Online]. Available: http://www.cfd-online.com/Wiki/SST_k-omega_model.

- [16] D. Chatterjee and K. Chatterjee, "Wall-Bounded Flow and Heat Transfer Around a Circular Cylinder at Low Reynolds and Hartmann Numbers," *Heat Transfer - Asian Research*, vol. 42, pp. 133-150, 2013.
- [17] D. Fiala, "Dynamic Simulation of Human Heat Transfer and Thermal Comfort," De Montfort University, Leicester.
- [18] Y. Zhang and T. Yang, "Simulation of human thermal responses in a confined space," in *Proceedings of 11th International Conference on Indoor Air Quality and Climate*, Copenhagen, Denmark, 2008.
- [19] R. J. Dear, E. Arens, H. Zhang and M. Oguro, "Convective and radiative heat transfer coefficients for individual human body segments," *International Journal of Biometeorology*, vol. 40, no. 3, pp. 141-156, 1997.
- [20] S. Murakami, S. Kato and J. Zeng, "Numerical simulation of contaminant distribution around a modeled human body: CFD study on computational thermal manikin - part II," *ASHARE Trans*, vol. 104, pp. 226-233, 1998.
- [21] Wikipedia, "Péclet number," [Online]. Available: http://en.wikipedia.org/wiki/Peclet_number.
- [22] Wikipedia, "Nusselt number," [Online]. Available: http://en.wikipedia.org/wiki/Nusselt_number.
- [23] Wikipedia, "Prandtl number," [Online]. Available: http://en.wikipedia.org/wiki/Prandtl_number.
- [24] Wikipedia, "Rayleigh number," [Online]. Available: http://en.wikipedia.org/wiki/Rayleigh_number.
- [25] ANSYS Fluent 12.0 Theory Guide, "5.2.2 Natural Convection and Buoyancy-Driven Flows Theory," 2009. [Online]. Available: <https://www.sharcnet.ca/Software/Fluent12/html/th/node108.htm>.
- [26] Wikipedia, "Grashof number," [Online]. Available: http://en.wikipedia.org/wiki/Grashof_number.
- [27] R. P. Clark, "Human skin temperature and convective heat loss," in *Bioengineering, thermal physiology and comfort*, Elsevier, Amsterdam, 1981.
- [28] E. A. Spiegel and G. Veronis, "On the Boussinesq approximation for a compressible fluid," American Astronomical Society, 1959.
- [29] Indian Institute of Technology Kanpur, "The Boussinesq approximation," 2003. [Online]. Available: <http://home.iitk.ac.in/~sghorai/NOTES/benard/node3.html>.
- [30] ANSYS Fluent 12.0 Theory Guide, "13.2.4 Natural Convection and Buoyancy-Driven Flows," 2009. [Online]. Available: <https://www.sharcnet.ca/Software/Fluent12/html/ug/node470.htm>.
- [31] G. R. Tabor, "ECM3111 Thermofluids Lecture Notes," University of Exeter, 2011.
- [32] G. R. Tabor, "ECMM106 Computational Modelling Lecture Notes," University of Exeter, 2013.

- [33] CFD Online, "Turbulence Modelling," 2013. [Online]. Available: http://www.cfd-online.com/Wiki/Turbulence_modeling.
- [34] CFD Online, "K-epsilon models," 2013. [Online]. Available: http://www.cfd-online.com/Wiki/K-epsilon_models.
- [35] Wikipedia, "Law of the wall," 2013. [Online]. Available: http://en.wikipedia.org/wiki/Law_of_the_wall.
- [36] Wikipedia, "Skin friction coefficient," 2011. [Online]. Available: www.cfd-online.com/Wiki/Skin_friction_coefficient.
- [37] GrabCAD, "GrabCAD," 2013. [Online]. Available: <http://grabcad.com/>.
- [38] The Engineering Toolbox, "Air Properties," 2013. [Online]. Available: http://www.engineeringtoolbox.com/air-properties-d_156.html.
- [39] ANSYS Fluent 12.0 Theory Guide, "13.2.2 Solution Strategies for Heat Transfer Modeling," 2009. [Online]. Available: <https://www.sharcnet.ca/Software/Fluent12/html/ug/node468.htm>.
- [40] J. Srebric, V. Vukovic, G. He and X. Yang, "CFD boundary conditions for contaminant dispersion, heat transfer and airflow simulations around human occupants in indoor environments," *Building and Environment*, vol. 43, pp. 294-303, 2008.
- [41] David LaserScanner, "David LaserScanner," [Online]. Available: <http://www.david-laserscanner.com/>. [Accessed 2012].
- [42] N. Martinho, A. Lopes and M. Gameiro de Silva, "Evaluation of errors on the CFD computation of air flow and heat transfer around the human body," *Building and Environment*, vol. 58, pp. 58-69, 2012.
- [43] R. Zhang, R. Nelson and J. Griffin, "Turbulence-Cylinder in Cross Flow," 2013. [Online]. Available: <https://sites.google.com/site/me2652012/turbulence-cylinder-in-cross-flow>.

10 Appendices

10.1 Appendix A: set-up of Linux-based computers

In order to gain the full potential of ANSYS Fluent on the high-powered Linux CFD research machines, it was necessary to set the following parameters:

1. To enable the use of multiple processors, Fluent Parallel needs to be enabled, with the maximum number of 4 cores selected.
2. The following must also be selected under Additional Settings:
 - a) ethernet under Interconnects
 - b) openmpi under MPI Types
 - c) SSH under Remote Spawn Command
3. Turn off hyper-threading (also known as multi-threading):

ANSYS Educational can use a maximum of 4 processes within Fluent Parallel. Therefore, if hyper-threading is switched on, which is where each processing core has multiple threads within it, ANSYS uses a maximum of 4 of these threads. If each core has two threads, this equates to the processing power of 2 whole processing cores, rather than 4 whole cores if hyper-threading is switched off.

Therefore it is recommended that hyper-threading is kept switched off in order to run simulations at the maximum speed of the computer.

10.2 Appendix B: risk assessment for use of line-laser

Department responsible: ENGINEERING	
Overall course title: ECMM102 Group Project	
Experiment dates: March 2013 to April 2013	
Locations: Room 261, Harrison Building, CEMPS, University of Exeter Room 218, Harrison Building, CEMPS, University of Exeter	
Project Description: Surface scanning of a miniature Manikin	
ACTIVITY	POTENTIAL HAZARD
Scanning of a miniature Manikin using a 5mW eye-safe line-laser	<p>Risk of eye damage if line-laser is pointed directly into eyes for a prolonged period</p> <p>Risk control measures:</p> <p>Always point laser away from eyes and avoid accidental reflection in glass or other reflective surfaces.</p> <p>Protective goggles deemed unnecessary.</p>

10.3 Appendix C: using the David Laserscanner software

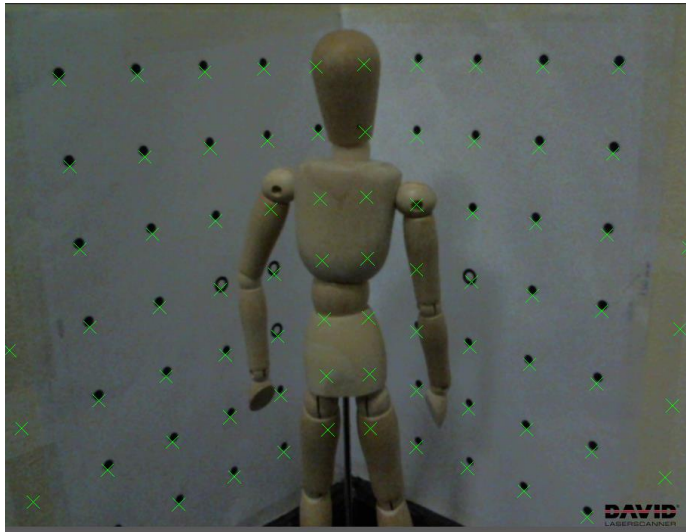


Figure 10.1: David Laserscanner calibration

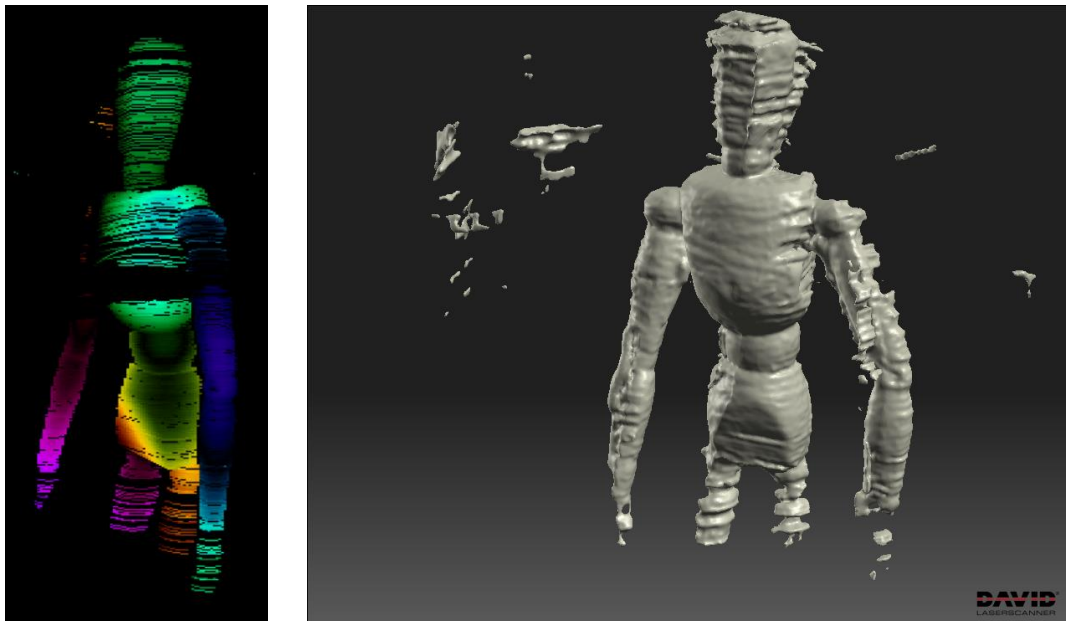


Figure 10.2: lines indicating detected surfaces coloured by distance from the camera (left); final aligned scan using several angles of the miniature Manikin (right)

10.4 Appendix D: sustainability and economic benefit

The resources used in this section of the group were almost solely the University teaching computers with only minor use of the specialist equipment of the thermal imaging camera and the David Laserscanner. Although the CFD simulations require high computing processing power for long-running simulations, the high use of electrical energy should be minimal compared with the ultimate benefit from the research if it is applied, especially in the view expressed in the Fourth Assessment Report of the IPCC that the buildings sector has the greatest potential for climate change mitigation [4]. Consequently, the economic benefit of the adoption of natural ventilation in buildings could be very significant. The overall costs of this project were well within the budget allowed.